Variation of the Schwabe cycle length during the grand solar minimum in the 4^{th} century BC deduced from radiocarbon content in tree rings

Kentaro NAGAYA

Solar-Terrestrial Environment Laboratory,
Nagoya University

March 6, 2012

Abstract

Solar activity alternates between active and quiet phases with an average period of 11 years, and this is known as the Schwabe cycle, which is clearly seen in the record of the sunspot number. Additionally, solar activity occasionally falls into a prolonged quiet phase of approximately 100 years (grand solar minima), as represented by the Maunder Minimum in the 17^{th} century, when sunspots were almost absent for 70 years and the length of the Schwabe cycle increased to 14 years.

Atmospheric carbon-14 concentration is an indirect index of the solar activity and carbon-14 is stored in tree ring annually. To examine the consistency of the characteristics of the Schwabe cycle among the several grand solar minima, the carbon-14 contents in single-year tree rings which were growing during the grand solar minimum of the 4^{th} century BC by using accelerator mass spectrometers.

The signal of the Schwabe cycle was detected with a statistical confidence level of higher than 95% by wavelet analysis. This is the oldest evidence for the Schwabe cycle at the present time, and the cycle lengths very likely increased to around 16 years during the BC4 minimum. Present study confirms the association between the long-term declination of solar activity and the increase of the Schwabe cycle length more strongly.

Grand solar minima, which are classified according to their duration time, may have different patterns of the variation with respect to the Schwabe cycle length. Increase of the cycle length during the grand solar minima may confirm the reproduction of prolonged sunspot absence using the flux transport dynamo model by Karak (2010).The sequence of the grand solar minima in the 8^{th} century BC and the 4^{th} century BC may have influenced the Earth's cooling period, similar to the Little Ice Age.

Contents

Chapter 1

Introduction

The Sun is one of the greatest factor which forms the Earth's environment where various kind of creatures including ourselves are living. The solar activity has been impacting on our life by varying in short term and long term relative to our lifetime. In the short term, large flares have caused the troubles of satellites in near-earth orbit (e.g., decreasing science satellite life in 2000, bad condition of satellite broadcasting in 1994, and possible decreasing for the accuracy of global positioning system), troubles of shortwave communication (e.g., the failure of aircraft radio in 2001), and the large-scale blackouts in Canada and North America in 1973, 1989, and 2003. The occurrence frequency of flares and sunspot number varies along with the solar activity. Solar short-term activities are observed directly from the ground and space satellites using telescopes at the present day. The sunspot number started to have been observed since the beginning of the 17 th century. It has been contin-

uously varying with an average period of 11 years since the middle of the 18^{th} century. Solar troubles have been often caused coincidentally with such a 11-years solar variation. On the other hand, long-term solar variation may have strongly impacted on the global environment. The reconstructed variation of historical temperatures indicates the warm period of Medieval Warm Period (MWP), which lasted during the 10-13^{th} century, and cool period of Little Ice Age (LIA), which lasted during the 13-19^{th} century, at the various countries around the world (Eddy, 1976; Jansen et al., 2007; and references therein). Little Ice Age is associated with the sequence of the long-term declines of solar activity. Furthermore solar activity possibly may link to even health and disease of creatures (Joseph and Wickramasinghe, 2010; Wainwright et al., 2010), since the UV rays in solar radiation act as microbicidal function in the upper atmosphere. The Sun has shown slightly different behavior in the cycle 23 compared with the recent cycles. It is concerned whether the Sun is approaching the next long-term decline phase. Studies for characteristics of the short-term behavior of the Sun before and during the long-term decline phase are required. The histories of solar variation have been studied by using indirect proxies of solar activity, which are stored in terrestrial archives. For example, carbon-14 concentration in old tree rings and beryllium-10 content in ice cores have been often used. In this thesis, the record of carbon-14 concentrations in tree rings which were growing during the ancient solar long-term decline is obtained as an indirect proxy of solar variation, and characteristic behaviors of the

11-years periodic activity of the Sun are studied.

Chapter 2

Review of the Schwabe cycle and grand solar minima

2.1 Solar cycle and the Maunder Minimum

Solar activity has been varying with an average cycle of 11 years, as is indicated by the solar radio flux, frequency of solar flare occurrence, the sunspot number, and so on. Various solar cycle indexes are shown in Figure 2.1 (p 6). The number of sunspots has been observed for approximately 400 years, and an 11-year periodicity is clearly evident from the early 18^{th} century to the present. The oldest record of the sunspot number traces back to 1600 AD as shown in Figure 2.2 (p 7) (Hoyt and

Schatten, 1998). This periodicity was found by Schwabe (Schwabe, 1843) and is referred to as the Schwabe cycle. The maximum (minimum) of sunspots corresponds to the maximum (minimum) solar magnetic activity.

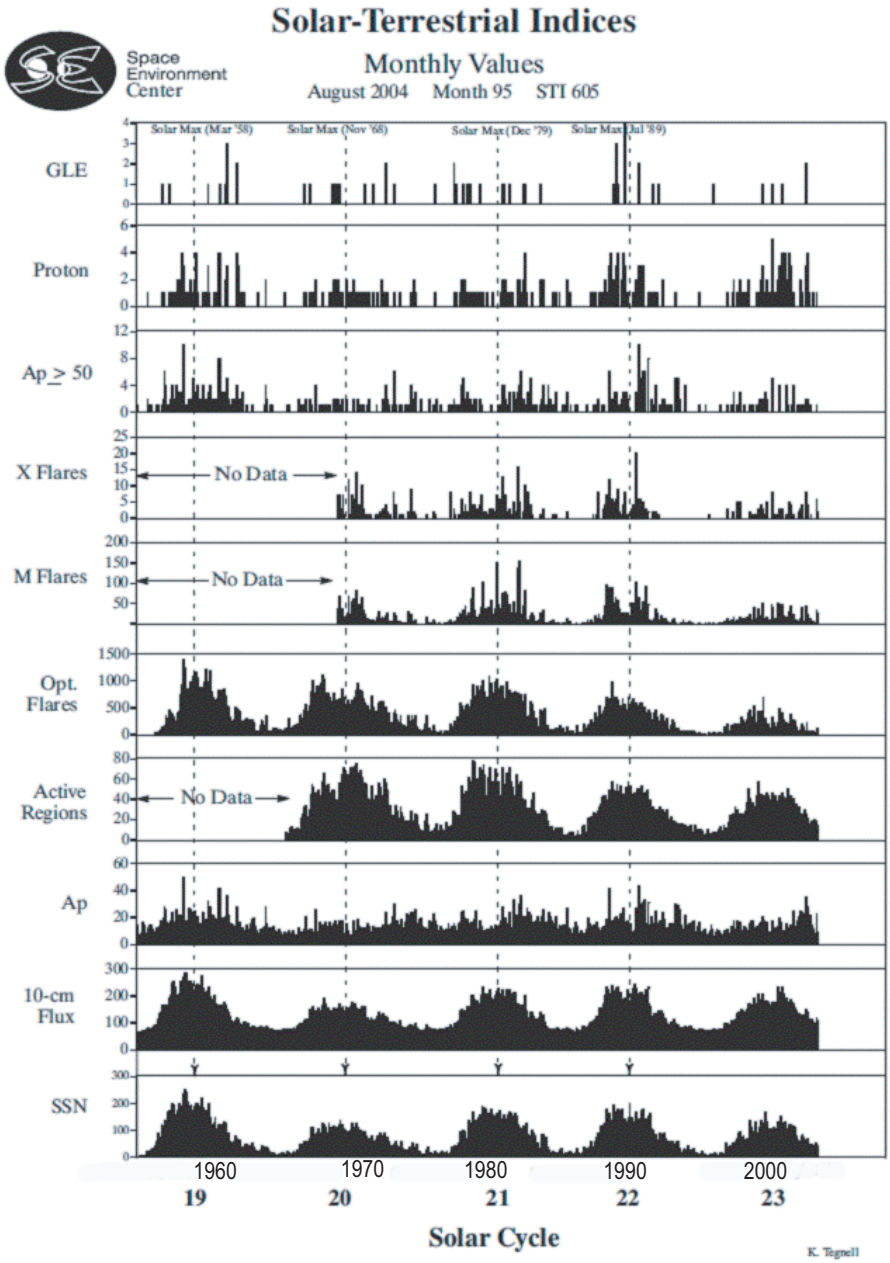

Figure 2.1: Monthly solar indices for solar cycles 19 through 23 (1954-2004 AD) (SWO PRF 1515, 2004). In descending order, they are the frequency of the ground level enhancements of cosmic ray flux from the sun (GLE), the frequency of the proton events, the frequency of Ap $\geq$ 50 (Ap: daily average of the geomagnetic disturbance at mid-latitudes in nT), the frequency of the X-class flares, the same but M-class flares, the same but optical flares, active regions, the Ap index, the flux of the 10.7 cm solar radio waves, and sunspot numbers.

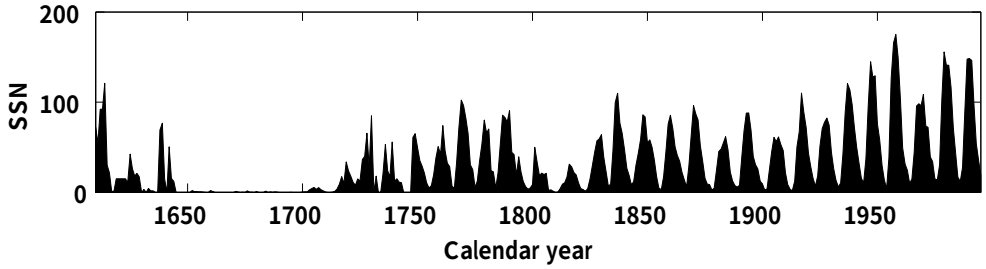

Figure 2.2: Annual sunspot number (SSN) from 1610 to 1995 AD (Hoyt and Shatten, 1998).

The Sun's dipole magnetic polarity inverts at every solar maximum of the Schwabe cycle, so that the solar magnetic state returns to the original state every 22 years (Hale et al., 1919; Hale and Nicholson, 1925; Babcock, 1959), and this cycle is known as the Hale cycle. The Schwabe and Hale cycles of solar magnetic activity can be reproduced, for example, using the flux transport dynamo model (Dikpati and Charbonneau, 1999; Hotta and Yokoyama, 2010), which applies the Babcock-Leighton model (Babcock, 1961; Leighton, 1964). Solar rotation is the differential rotation. Angular velocity of solar convection zone increases from pole toward equator. Additionally, solar plasma circulates on meridional cross-section of the solar convection zone. The direction of the circulation is from the equator toward the pole at the surface layer and return to the equator in the deep layer. Solar dipole magnetic field (poloidal field) is elongated toward the rotation direction due to the differential rotation, and change to toloidal field (Ω effect, Figure 2.3 (a), (b), p 8). Toroidal field partially rise up to the surface of the convection zone by magnetic pressure, and forms loops of the magnetic line. Since the loop

of the magnetic line is twisted by 90 degrees by the Coriolis force when it rise up to the surface, the magnetic loop is opposite direction relative to the original poloidal field (α effect, Figure 2.3 (c)-(f), p 8). Sunspot is produced around the foot of these magnetic loops. Flare often occurs by the reconnection of these magnetic loops. These magnetic loops are transfered to the polar region by meridional circulation, and cancel the original magnetic field, and finally the sun's dipole magnetic polarity is inverted (Figure 2.3 (g)-(i), p 8).

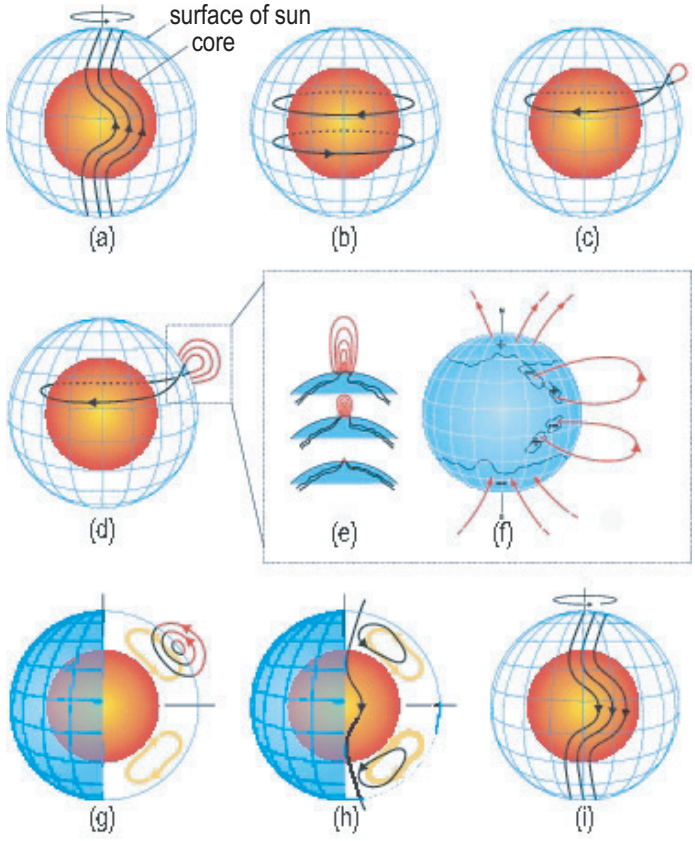

Figure 2.3: Diagram of the Babcock-Leighton model (Dikpati, 2008). The orangy sphere represents the radiative zone of the sun, the blue sphere represents the surface of the sun, spherical shell between above two sphere is the convection zone, the black line and arrow represents the magnetic field lines, and yellow line represents the meridional circulation.

In addition to the Schwabe cycle and the Hale cycle, the Sun has exhibited long-term weakening, such as during the period from 1645 to 1715 AD (Figure 2.2, p 7) (Hoyt and Shatten, 1998), known as the Maunder Minimum, one of the grand solar minima (Eddy, 1976). The Maunder Minimum is associated with the Little Ice Age (LIA), when the Earth was cooled by approximately 1 °C on a global average during the 13-19th centuries (Eddy, 1976). The number of sunspots constantly recorded since the middle of the 18th century shows that the Schwabe cycle length has been fluctuating at around 11 years (Watari, 2008; Richards et al., 2009) with a standard deviation of $\pm$1.2 year. The Schwabe cycle lengths that has been studied by Richards et al. (2009) is shown in Table 2.1 (p 10). It is suggested that there is the inverse correlation between the Schwabe cycle length and the amplitude of the sunspot number record (Figure 2.4, p 11) (Solanki et al., 2002; Hathaway et al., 2002; Watari, 2008). The radiocarbon (carbon-14) concentration in tree rings can also be used to study the variability of solar cycle lengths, such as a prolonged absence of sunspots or prior to records of the sunspot number, and in grand solar minima other than the Maunder Minimum during the observational era.

Table 2.1: The solar cycle numbers, years of solar minima, the cycle lengths from solar minima, years of solar maxima, and the cycle lengths from solar maxima (Richards et al., 2009).

Cycle No.	Minimum	Length	Maximum	Length
1	1755.2	11.3	1761.5	8.2
2	1766.5	9.0	1769.7	8.7
3	1775.5	9.2	1778.4	9.7
4	1784.7	13.6	1788.1	17.1
5	1798.3	12.3	1805.2	11.2
6	1810.6	12.7	1816.4	13.5
7	1823.3	10.6	1829.9	7.3
8	1833.9	9.6	1837.2	10.9
9	1843.5	12.5	1848.1	12.0
10	1856.0	11.2	1860.1	10.5
11	1867.2	11.7	1870.6	13.3
12	1878.9	10.7	1883.9	10.2
13	1889.6	12.1	1894.1	12.9
14	1901.7	11.9	1907.0	10.6
15	1913.6	10.0	1917.6	10.8
16	1923.6	10.2	1928.4	9.0
17	1933.8	10.4	1937.4	10.1
18	1944.2	10.1	1947.5	10.4
19	1954.3	10.6	1957.9	11.0
20	1964.9	11.6	1968.9	11.0
21	1976.5	10.3	1979.9	9.7
22	1986.8	9.7	1989.6	10.7
23	1996.5		2000.3	
average		11.0±1.2		10.9±2.1

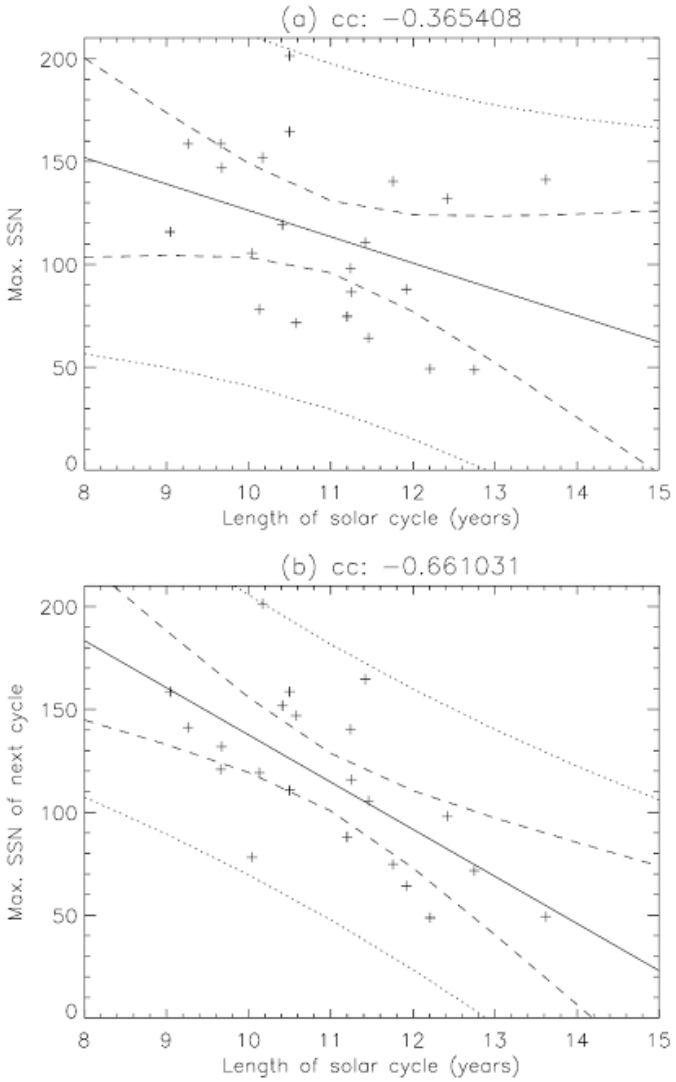

Figure 2.4: The relationship between the cycle length and the maximum SSN (upper) or the maximum SSN in the next cycle (lower). The solid line shows the result of the least square fitting. The two dotted curves are the 95% confidence intervals for observed values while the two dashed curves are the 95%confidence intervals for expected values. The correlation coefficient is -0.365 (upper) and -0.661 (lower) (Watari, 2008).

2.2 Carbon-14 as an indirect index of solar activity

Radiocarbon (carbon-14) is a cosmogenic nuclide that has a half-life of 5,730 (±40) years (Godwin, 1962). It is produced by a process where thermal neutrons of secondary cosmic rays are captured by atmospheric nitrogen nuclei in the stratosphere and the upper troposphere (Figure 2.5, p 13). When solar magnetic activity is low, more of the low energetic (ca. <10 GeV) galactic cosmic rays can enter the heliosphere, and thus the carbon-14 production rate in the atmosphere increases. Therefore, both the cosmic-ray flux at the earth and atmospheric carbon-14 which is produced by cosmic-ray are good indexes of solar activity. Both the cosmic-ray flux and atmospheric carbon-14 concentration are inversely correlated with the solar activity. The effect of the Schwabe cycle on cosmic-ray flux is reflected in the ground-level neutron monitor count, which has been varing with an average period of 11 years (Figure 2.6, p 14) (ICRU, 2010). In addition to the Schwabe cycle, the shape of the time profile of cosmic-ray flux varies alternatively between broad-top and sharp-top peaks, which is attributed to the Hale cycle (Figure 2.6, p 14) (Kota and Jokipii, 1983). Carbon-14 produced is oxidized to $^{14}CO_2$, which circulates around the earth in the atmosphere. Some CO_2 is absorbed by photosynthesis at the land surface to form tree rings every year (Figure 2.5, p 13). At the same time, atmospheric $^{14}CO_2$ diffuses into the ocean and the biosphere over a time scale of several decades.

Thus, the time series of carbon-14 concentration in tree rings records the solar 11-year variation back to more than several thousand years ago. However, it must be noted that carbon-14 records from tree rings can represent not only solar activity, but also other erratic noise components such as climatic noise.

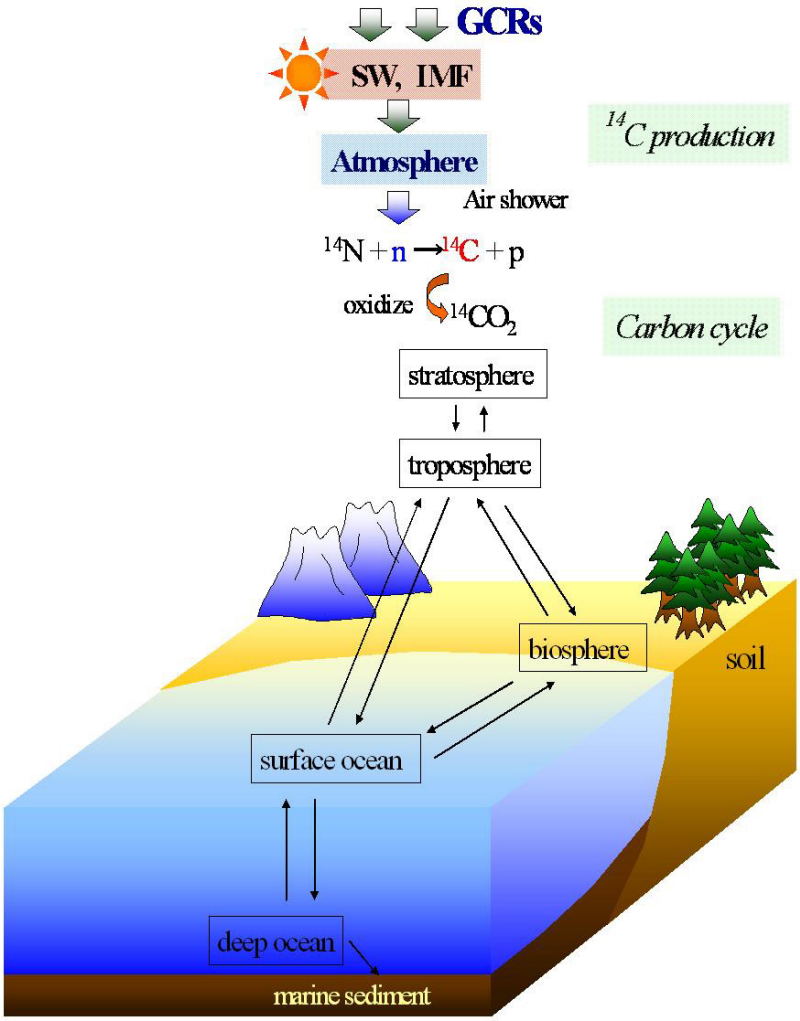

Figure 2.5: Diagram of the ^{14}C production and global circulation (this diagram is privately provided from H.Miyahara).

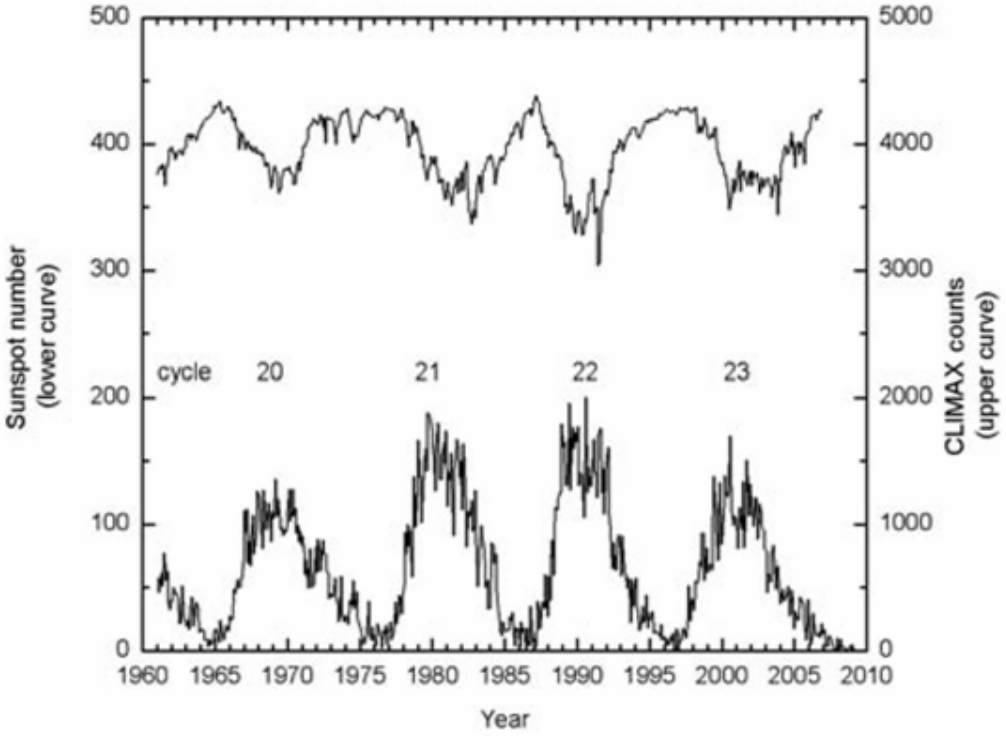

Figure 2.6: Sunspot number (lower curve) and monthly averaged Climax neutron monitor counts (counts per hour divided by 100) for solar cycles 20 through 23 (from 1964 to beginning of 2009) (ICRU, 2010).

2.3 Grand solar minima in the past

The grand solar minima are periods of prolonged sunspot absences, which is estimated as the periods when the carbon-14 production rate exceeds the threshold level corresponding to the prolonged sunspot absence in the Maunder Minimum as shown by a horizontal line in Figure 2.7 (p 15) (Stuiver and Quay, 1980). The summary of decadal carbon-14 records, IntCal (Stuiver et al., 1998; Reimer et al., 2004; 2009), indicates the quasi-periodic occurrence of several grand solar minima (carbon-14 max-

ima) during the past 10000 years (Figure 2.8, p 16) (Stuiver and Braziunas, 1989; Usoskin et al., 2007). Grand solar minima are divided into two types according to their duration time; the Spörer-type (S-type) of long duration time, and the Maunder-type (M-type) of short duration time (Stuiver and Quay, 1980; Stuiver and Braziunas, 1988; Stuiver,1991). In addition, the shortest duration time of the Wolf-type (W-type) is defined as the third type of grand solar minima by Goslar (2003) (Figure 2.9, p 17).

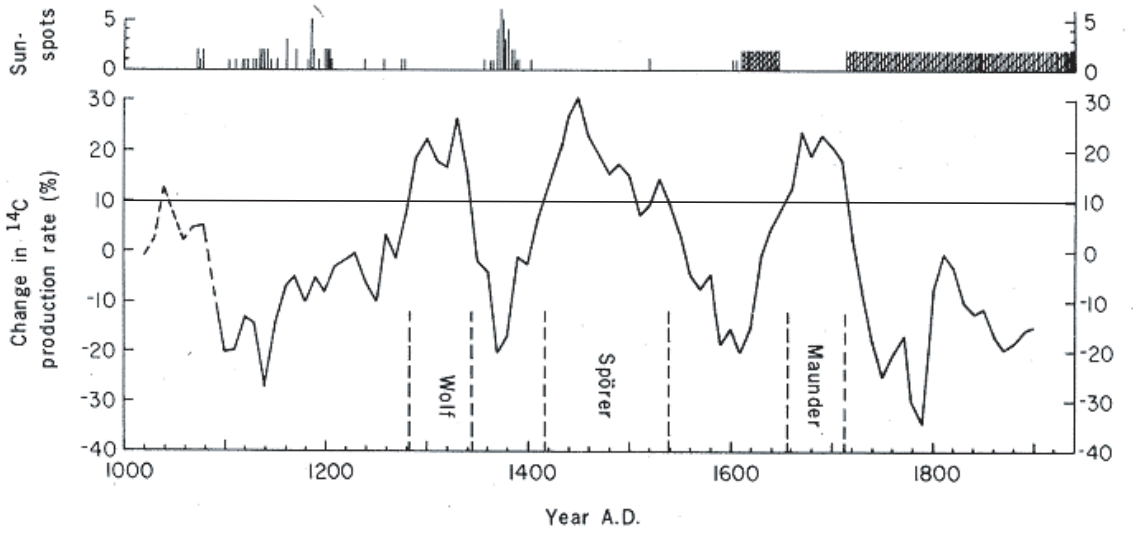

Figure 2.7: The definition of grand solar minima (Stuiver and Quay, 1980). Upper plot represents the sunspot numbers, and lower plot represents the ^{14}C production rate relative to the average value.

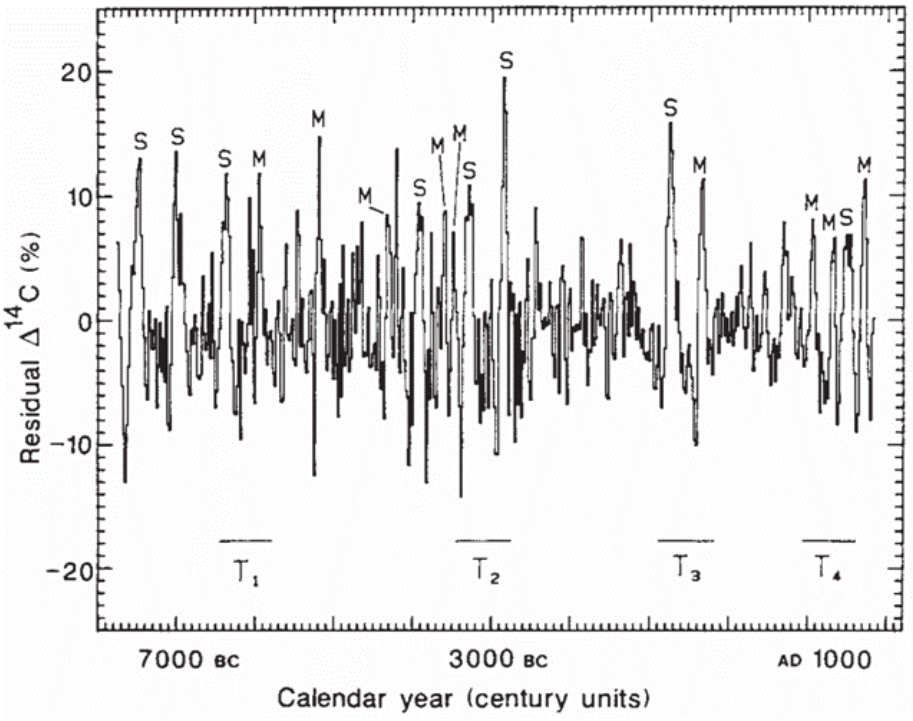

Figure 2.8: Atmospheric ^{14}C concentration anomaly of the last 10000 years (Stuiver and Braziunas, 1989). The "S" and "M" represent the types of grand solar minimum (^{14}C maxima).

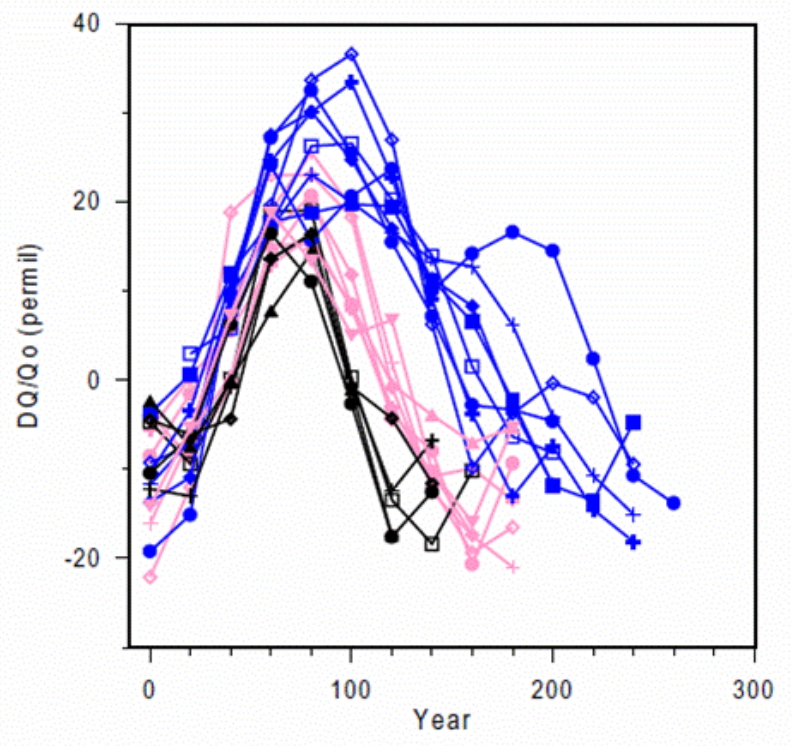

Figure 2.9: Comparison of ^{14}C peaks between the three types of grand solar minima (Goslar, 2003). The y-axis represents the ^{14}C production rate anomaly and x-axis represents the time from the onset of the ^{14}C increase. Blue plots represent the Spörer-type, pink plots represent the Maunder-type, and black plots represent the Wolf-type.

Over the last 3000 years, two S-type minima, two M-type minima, and three W-type minima have been recorded in IntCal (represented as (a)-(g), in Figure 2.10, p 18). In reverse chronological order, they are (a) the Dalton Minimum (W-type; 19^{th}century AD), (b) the Maunder Minimum (M-type; 17-18^{th}century AD), (c) the Spörer Minimum (S-type; 14-16^{th}century AD), (d) the Wolf Minimum (W-type; 13-14^{th}century AD), (e) the Oort Minimum (W-type; 11-12^{th}century AD), (f) the BC4 Minimum (M-type; 4-3^{th}century BC), and the (g): the BC8 Minimum (S-

type; 9-7^{th}century BC). The sequence of the Wolf Minimum, the Spörer Minimum, and the Maunder Minimum may have related to the LIA in the past millenium (Figure 2.11, p 19). In addition to the LIA, climatic cooling and/or a shift towards wetter conditions is indicated around the 8^{th} century BC, which is associated with the BC8 Minimum (Geel et al., 1996; Plunkett and Swindles, 2008). Some works indicate that this climatic event around 8^{th} century BC may have extended to include the period of the BC4 Minimum (Desprat et al., 2003; Barber and Langdon, 2007; Swindles et al., 2007; Garcia, Santisteban and Lopez-Pamo, 2007; Berner et al., 2008).

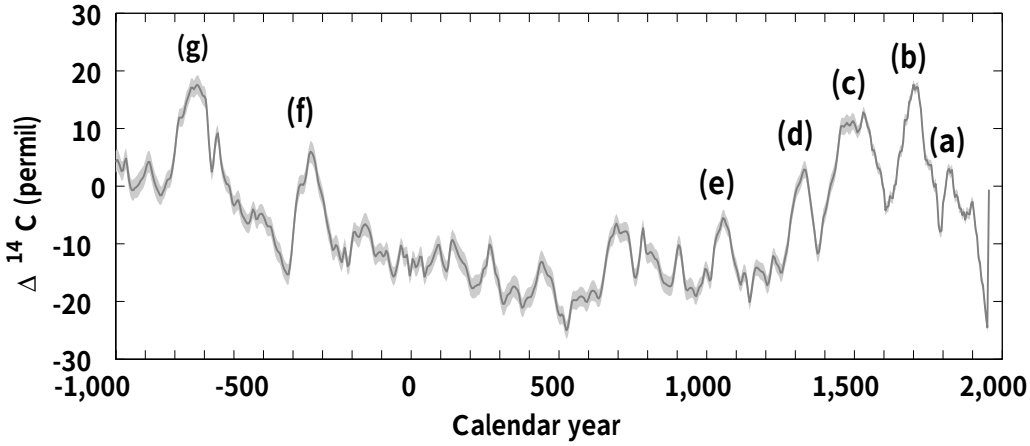

Figure 2.10: Decadal carbon-14 record (IntCal09) of the last 3000 years. The gray area represents the error, (a)-(g) corresponds to the seven grand solar minima (carbon-14 maxima).

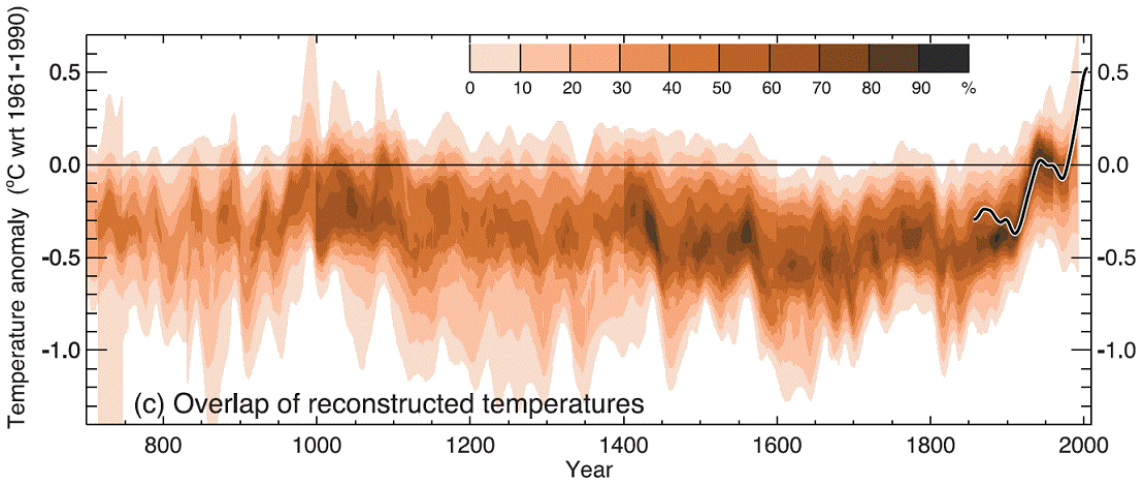

Figure 2.11: Reconstructed northern hemispheric temperature of the last 1000 years (Jansen et al., 2007). Color scale represents the overlap of the published multi-decadal time scale uncertainty ranges of 10 temperature reconstructions.

2.4 Reconstruction of the Schwabe cycle

To study the variation of the Schwabe-cycle length in the past, the solar variability in the past must be traced with a time resolution better than a few years, using accurately dated samples. Carbon-14 in tree rings can therefore be a strong tool for this purpose. However, the variations in the carbon-14 production rate in the stratosphere are attenuated, because the atmospheric carbon-14 content is much larger than the amount of carbon-14 production. The attenuation rate and time lag for 11-year variations are estimated to be approximately 1/100 and several years, respectively, according to the carbon cycle model (Siegenthaler and Beer, 1988) (Figure 2.12, p 20).

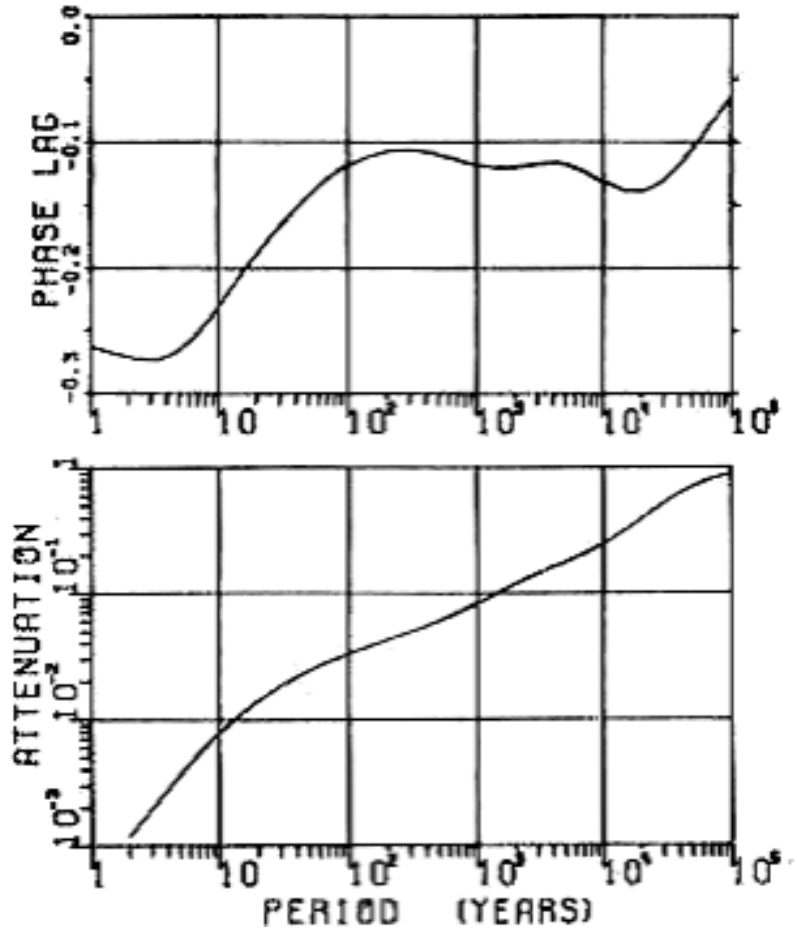

Figure 2.12: Simulated attenuation rate (lower) and phase lag (upper) between the input (the periodical change of the ^{14}C production rate) and the output (the atmospheric ^{14}C concentration). The x-axis represents the period. The phase lag is represented by the ratio relative to the x value.

The average carbon-14 production change attributed to the Schwabe cycle in 1953-1995 AD is approximately ±15% (Masarik and Beer, 1999); therefore, the amplitude of variation in the atmospheric carbon-14 concentration is estimated to be approximately 1.5‰. The amplitude of atmospheric carbon-14 concentration in the 10^{th} century (Miyahara, Yokoyama, and Masuda, 2008), 14^{th} century (Miyahara et al., 2010), and 17^{th} century (Stuiver et al., 1998; Miyahara et al., 2004; Miyahara et al., 2010),

and the 18-20^{th} century (Stuiver et al.,1998) from observations is 1-3‰. The difference of amplitude between estimation and observation may indicate a temporal variation of the amplitude of cosmic-ray variation due to the Schwabe cycle. However, the statistical error of carbon-14 concentration in the case of measurement using the accelerator mass spectrometer (AMS) at Nagoya University or the University of Tokyo is approximately 3-5‰. Therefore, due to the critical signal/noise ratio, it is difficult, if not impossible, to investigate the Schwabe cycle features from carbon-14 records.

The concentration of beryllium-10 (^{10}Be) in ice cores, which is also a cosmogenic nuclide, shows that the Schwabe cycle persisted throughout the Maunder Minimum (Beer, 1998; Berggren et al., 2009). Carbon-14 and beryllium-10 are incorporated into natural archives by different processes. The mean residence time of beryllium-10 in the atmosphere is approximately 1-2 years, which is shorter than that of carbon-14, because ^{10}Be nuclei attach to aerosols and immediately fall to the land surface after production. Therefore, the ^{10}Be concentration in an ice core indicates the fluctuation in the rate of production more directly than carbon-14. However, the ^{10}Be concentration is affected by climatic and regional effects on the accumulation process of ^{10}Be. In addition, the annual dating of ice cores is difficult. Therefore, carbon-14 and beryllium-10 should be complementarily used to trace past solar activity.

2.5 Schwabe cycle length during the grand solar minima

In previous works, variations of the Schwabe cycle length in the Maunder Minimum (M-type) and the Spörer Minimum (S-type) were investigated using the carbon-14 method. Two independent studies of carbon-14 records by Stuiver et al. (1998) and Miyahara et al. (2004) indicate that the Schwabe cycle length increased to around 14 years in the Maunder Minimum (Miyahara et al., 2004). The length of the Schwabe cycle was about 10 years around 1605 AD (the onset of the ^{14}C increase), and considered to subsequently increase to 12-13 years around the onset of the prolonged sunspot absence, and maintained at about 14 years after 1660 AD (Miyahara et al., 2010) (Figure 2.13, p 24). The annual carbon-14 record for the Spörer Minimum has also shown an increase of the Schwabe cycle length to approximately 13 years, but only for the two preceding cycles before the onset of the estimated prolonged sunspot absence (Miyahara et al., 2010) (Figure 2.14, p 25). The variation of the Schwabe cycle length in the Dalton Minimum is studied from the record of the sunspot number. The preceding cycle is about 13 years, although only for a single cycle starting at around 1784 AD (Miyahara et al., 2010) (Figure 2.15, p 26). These works suggest the possibility that the Schwabe-cycle length could be an index of the long-term solar variability, and could be the foundation for the phenomenological prediction of grand solar minima. Further confirmation of the relation between the

grand solar minima and the increase of the Schwabe-cycle length is required, and investigation of the timing of the increase in the cycle length relative to the period of estimated sunspot absence for each type of grand solar minima is also required.

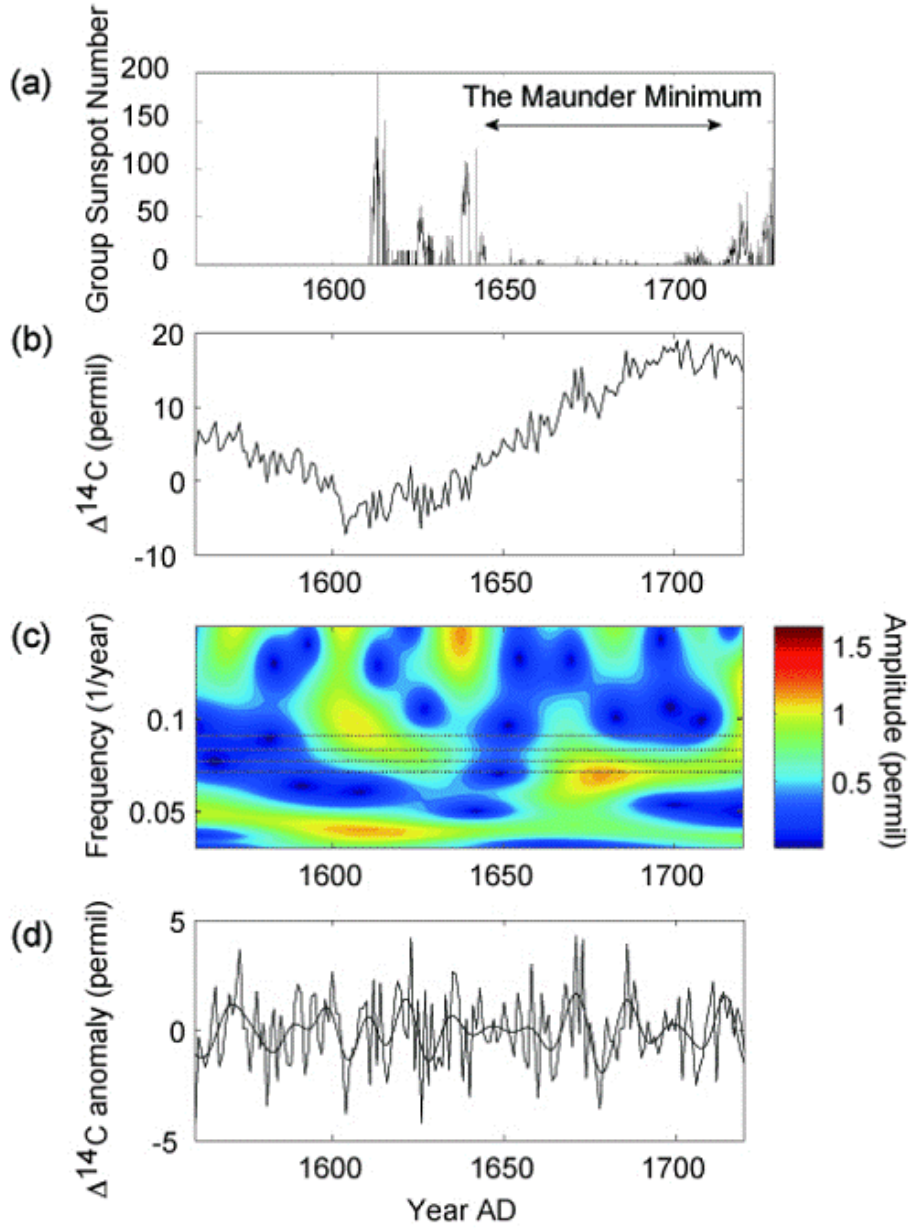

Figure 2.13: The suggestion for the increase of the Schwabe cycle lengths during the Maunder Minimum (Miyahara et al., 2010). (a): Record of the monthly sunspot number (Hoyt and Shatten, 1998). (b): Annual ^{14}C record (Stuiver et al., 1998). (c): The frequency spectrum by the wavelet analysis for (b). The horizontal lines correspond to periods of 11, 12, 13, and 14 years. (d): Bandpass filtered ^{14}C record with a band width of 1/25-1/10 (black solid line) and 1/25-1/1 (gray line) (year^{-1}).

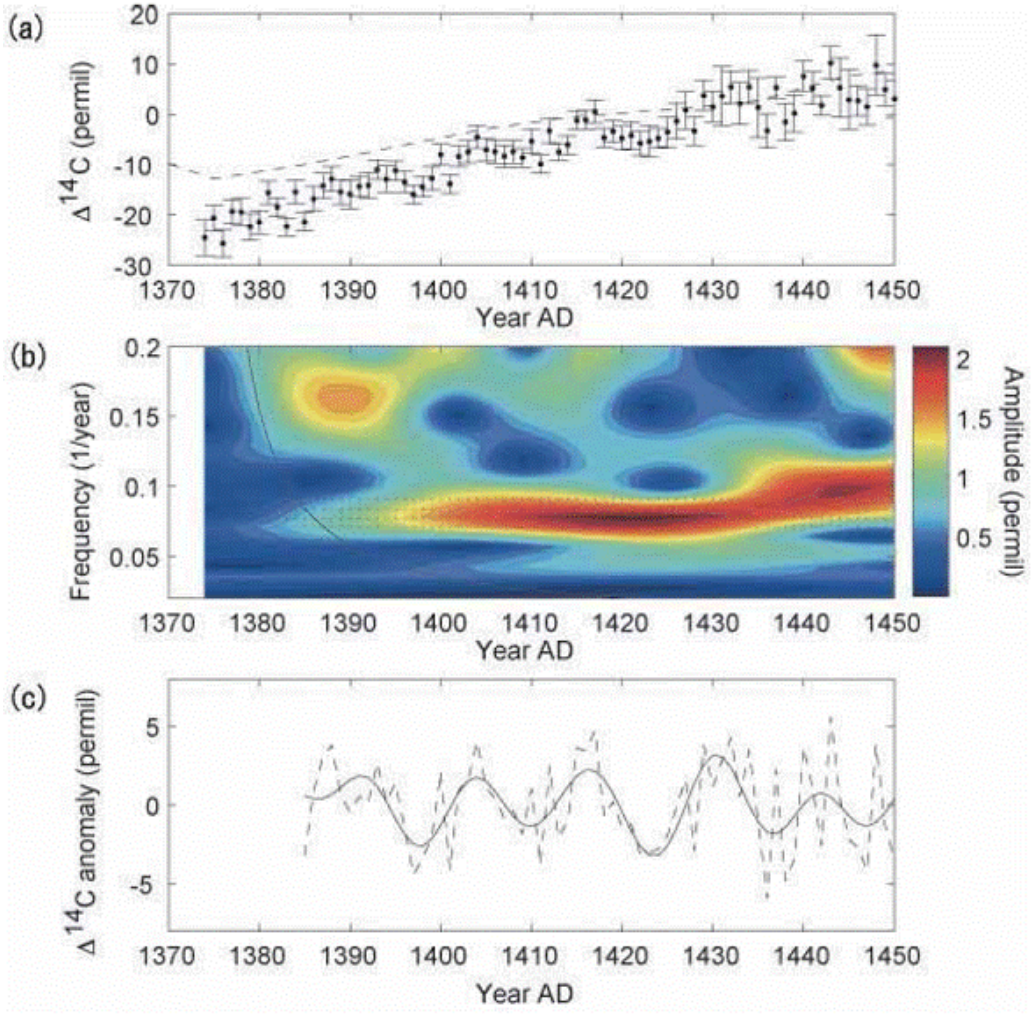

Figure 2.14: The suggestion for the increase of the Schwabe cycle lengths just before the Spörer Minimum (Miyahara et al., 2010). (a): The ^{14}C records at the Spörer Minimum. Dashed line represents the IntCal. Dots and error bars represent the annual ^{14}C record. (b): The frequency spectrum by the wavelet analysis for (a). (c): Bandpass filtered ^{14}C record with a band width of 1/25-1/1 (dashed line) and 1/25-1/10 (solid line) (year^{-1}).

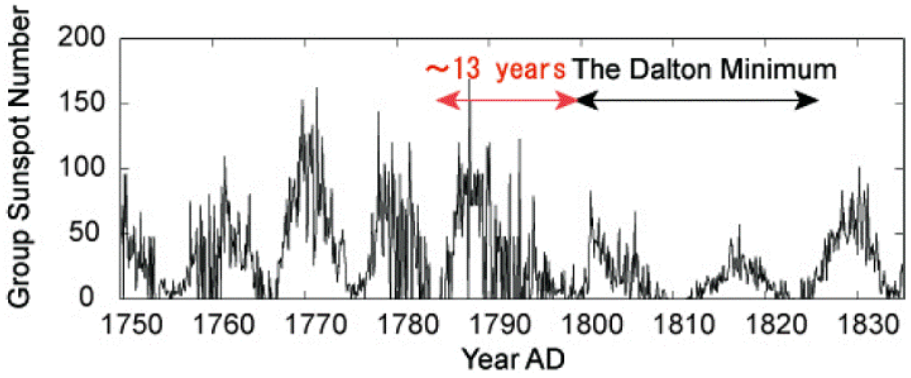

Figure 2.15: The record of the sunspot numbers (Hoyt and Schatten, 1998) around the Dalton Minimum (1795-1825 AD) (Miyahara et al., 2010).

2.6 Purpose of this study

In this paper, we study the variation of the Schwabe-cycle length in the grand solar minimum of the 4^{th} century BC (the BC4 Minimum). The statistical confidence level for detection of the Schwabe cycle from the carbon-14 record is also examined. The BC4 Minimum is one of the M-type minima. The decadal carbon-14 concentration starts to rise from 415 BC and reaches a maximum at 340 BC, then declines to the original level by 215 BC, as shown in Figure 2.16 (p 27). The estimated prolonged sunspot absence is approximately 400-320 BC, which is considered from the record of the carbon-14 production rate reported by Stuiver and Braziunas (1988). Theoretical implications of the trigger for the prolonged sunspot absence are discussed based on solar dynamo theory. The possible association of the long-term solar variation around the 4^{th} century BC and terrestrial cooling during this period is also discussed.

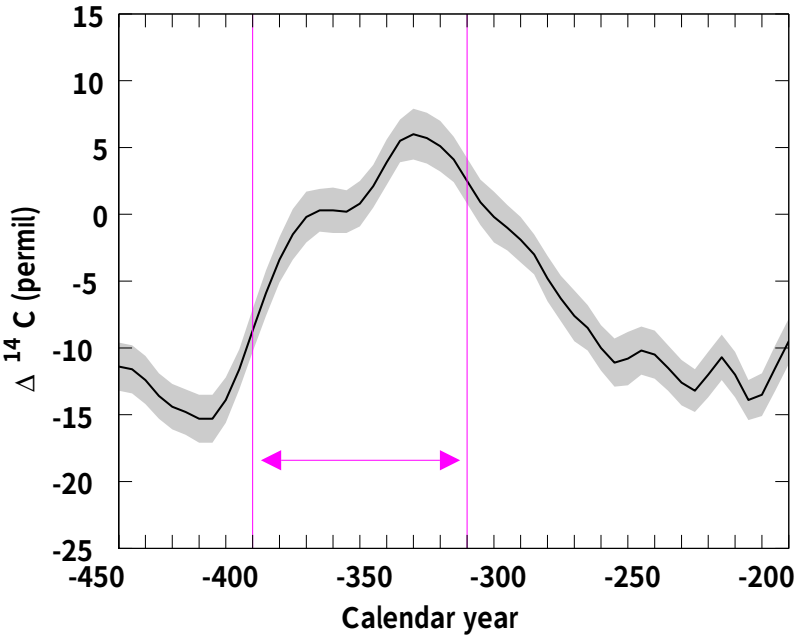

Figure 2.16: IntCal09 curve around 4^{th} century BC (Reimer et al., 2009). The period between the two vertical magenta lines represents the estimated prolonged sunspot absence.

Chapter 3

Measurement of the carbon-14 in tree rings

The carbon-14 concentration was measured using accelerator mass spectrometer (AMS). Prior to AMS measurement, the tree ring sample was chemically washed (pretreatment) and converted to graphite (target preparation), which is used as the target material for the AMS. The pretreatment and target preparation were carried out at Solar Terrestrial Environment Laboratory (STEL), Nagoya University, and AMS measurements were carried out at the Center for Chronological Research (CCR), Nagoya University and The Micro Analysis Laboratory Tandem Accelerator (MALT), the University of Tokyo. Detailed processes of measurements are stated in this chapter.

3.1 Sample

The sample for carbon-14 measurement was a camphor tree (Figure 3.1, p 29) excavated from the bottom of Fukushima River, Miyazaki in southern Japan (31.28 °N and 131.14 °E) in 1996; carbon-14 dating, in addition to botanical, topographical, and geological research, was conducted (Nagaoka et al., 1998). The basal diameter of the tree is 1.85 m, and its estimated age is approximately 500 years. The date of death was estimated to be around 70 BC by carbon-14 dating at the Center for Chronological Research (CCR), Nagoya University (Nagaoka et al., 1998). The sample tree had been growing during the 6-1th century BC which include the period of the BC4 Minimum. Then we have measured ^{14}C contents in each single-year tree ring by using AMS. We used NIST SRM4990C oxalic acid (new NIST) as the standard sample and the commercial oxalic acid (Wako Pure Chemical Industries, No. 159-00425) as the back ground (blank) sample.

Figure 3.1: The picture of the tree ring sample (camphor tree) used in this study. The basal diameter is 1.85 m and the estimated tree age is about 500 years.

3.2 Pretreatment

Constituents of wood are cellulose (60%), lignin (30%), and others such as resin (10%). Only cellulose component was chemically extracted from each tree ring by pretreatment, because other constituents possibly move between the tree rings. Firstly, the annual tree ring samples were separated individually by a cutter knife with great caution to contamination, and the biennial rings were then selected and washed with distilled water under ultrasonication to remove the dust attaches to the wood pieces. To remove other components such as resin, the samples were then treated using the A-A-A method, which is washing with HCl-NaOH-HCl solutions in this order at 60-70 °C for 8-10 hours in each stage of the process. The samples were then washed with a hydrochloric acid solution of sodium chlorite for 8-10 hours at 70-80 °C to remove lignin, and rinsed with distilled water. The samples and solutions were put in the vial containers and heated on the electric hot plate. For the thermal management, distilled water in the same vial container (dummy sample) was heated with wood samples and the water temperature was measured and maintained at ±5 °C. Typically, 5-40 mg of the cellulose is obtained from 100 mg of the wood sample, although the content rate of the cellulose is 60%. This is because a little sample is lost during the every exchange of the solution by using a pipette.

3.3 Target preparation

The cellulose from single tree rings and the oxalic acid (standard sample or back ground sample) were converted to the graphite target material. The 5 mg of the cellulose or 11 mg of the oxalic acid were encapsulated in a silica tube with an oxidant (1 g of copper oxide) and evacuated by the vacuum line A (Figure 3.2). The mixture was combusted at 850 °C (for cellulose) or 450 °C (for oxalic acid) for 3 hours to oxidize the cellulose or oxalic acid to carbon dioxide. The tube was connected to the vacuum line B and the carbon dioxide was purified using cold traps (Figure 3.3). The traps are the ethanol of -90 °C for removing water vapor, and the pentane of -130 °C (only for cellulose) for removing other extra gases such as sulfur oxide. The temperatures of the traps were monitored by thermocouple attached to the outside wall of the traps within the cooling media. Finally, the carbon dioxide was reduced to graphite using hydrogen in the presence of 2 mg of iron catalyst at 650 °C for 6 hours by using the electric oven (Figure 3.4, p 34). Typically, the conversion efficiency between cellulose and graphite is about 30% by our system in STEL. The produced graphite was then loaded and pressed into the target holder for the AMS measurement (Figure 3.5, p 34). Thus the graphite targets were produced from the annual tree-ring samples.

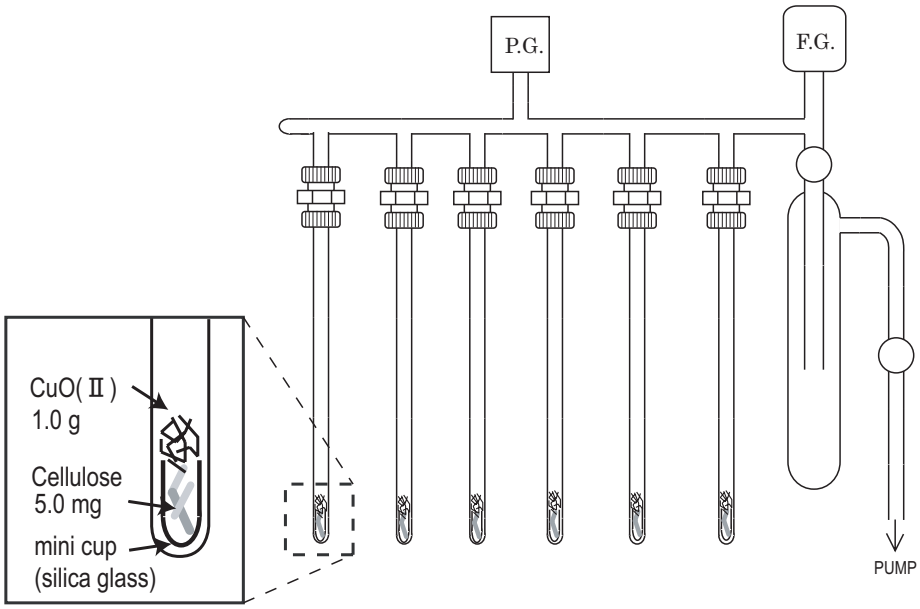

Figure 3.2: The vacuum line A at STEL. The pressure is measured by Pirani gauge (P.G.) and Full-rage gauge (F.G.).

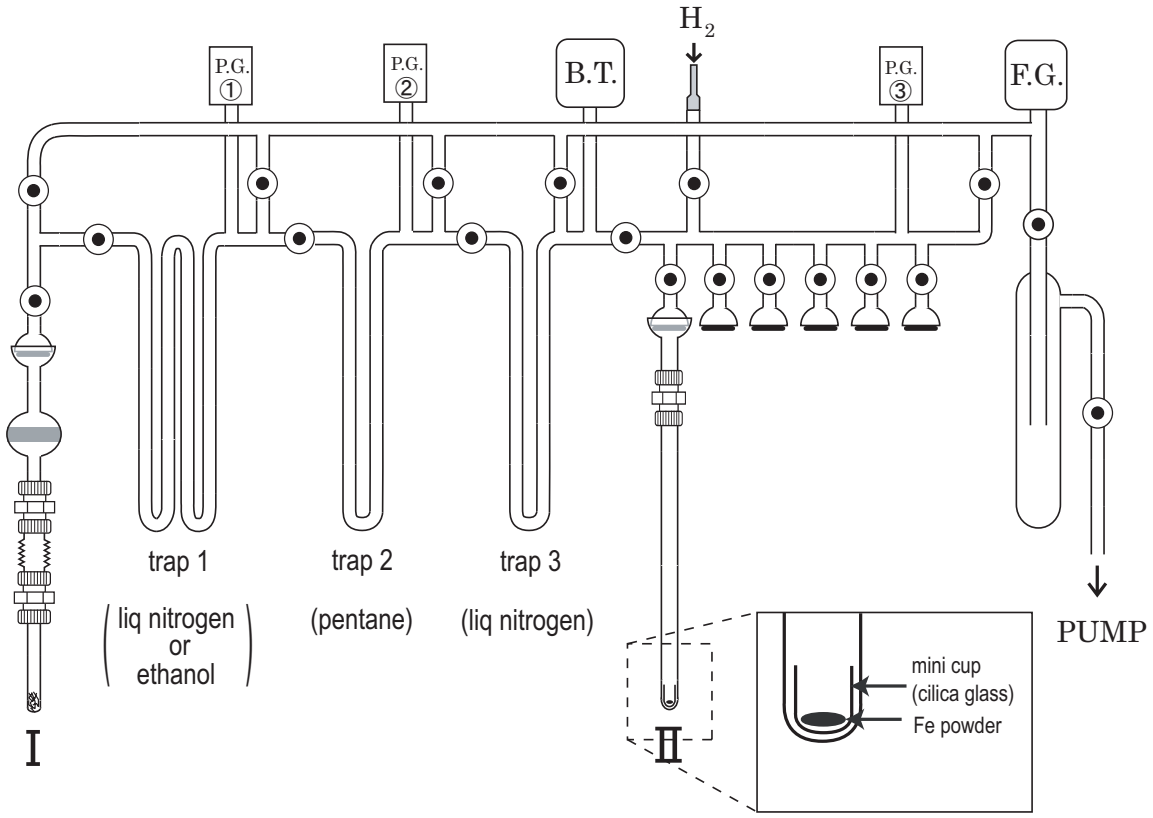

Figure 3.3: The vacuum line B for CO_2 purification at STEL. The gas is introduced from the position I. Water is trapped at the trap 1 by the ethanol at -90 °C, other extra gases are trapped at the trap 2 by the pentane at -130 °C (only for cellulose), amount of purified carbon dioxide is measured at the trap 3 by Baratron pressure gauge in gas phase, and encapsulated with hydrogen and iron powder as catalyst at the position II. The pressure of vacuum at each trap is measured by Pirani gauges (P.G. 1-3), Baratron (B.T.) and Full-range gauge (F.G.).

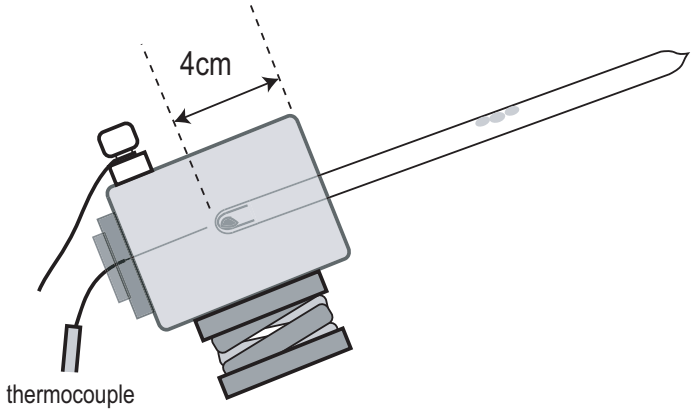

Figure 3.4: The apparatus for reduction of the carbon dioxide by using the small electric oven at STEL. The temperature is monitored by the thermocouple at the tip of the silica tube containing the carbon dioxide, hydrogen, and iron powder.

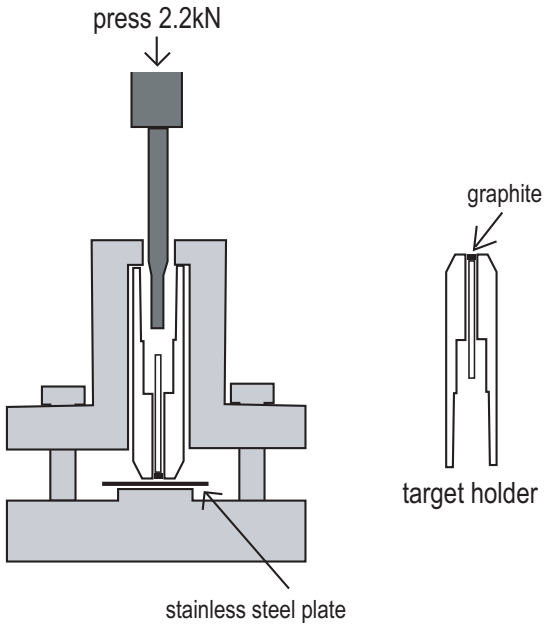

Figure 3.5: The structure of the target holder for the CCR AMS. The graphite sample is loaded at the tip of the target holder. The length of the target holder for the CCR AMS is about 4 cm.

3.4 Accelerator Mass Spectrometers (AMS)

Two different AMS systems were used in this study (one at the Center for Chronological Research (CCR) at Nagoya University (Nakamura et al., 2000) and the other at The Micro Analysis Laboratory Tandem Accelerator (MALT) at the University of Tokyo (Matsuzaki et al., 2007)). The principle of the measurement by AMS is that the graphite target is ionized and accelerated by high voltage, and the orbits of each ionized carbon isotope is separated by magnets due to the different mass, then the mass-analyzed ^{14}C is detected and counted, whereas currents are measured for ^{12}C and ^{13}C. The overall measurement errors were mainly dominated by the statistics of carbon-14 counts. The AMS at CCR and MALT are different in the specs and the operations.

3.4.1 The AMS at CCR, Nagoya University

The AMS at CCR is manufactured by HVEE (High Voltage Engineering Europe), Netherlands. The graphite targets (Figure 3.6, p 36) produced from annual tree-ring samples are set in the target wheel (Figure 3.7, p 36), and measured one by one in rotation. Here, measuring each target once around a wheel is defined as "1 run". The graphite targets set in the target wheel are sputtered by cesium ion and ionized to C^-. The graphite target is applied to the cathode and C^- is extracted as ion beam.

Figure 3.6: The picture of the target holder.

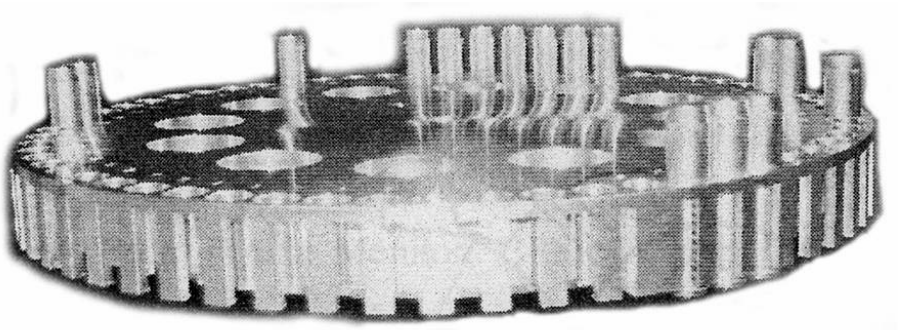

Figure 3.7: The picture of the target wheel for the CCR AMS.

Carbon isotopes, $^{12}C^{-}$, $^{13}C^{-}$ and $^{14}C^{-}$ are injected into accelerator simultaneously using a recombinator system where intensity of only $^{12}C^{-}$ is attenuated to 1/90 to avoid the overload of the accelerator because the ratio of ^{12}C to ^{13}C is about a hundred. Electrical potential is the highest at the central part (terminal) of the accelerator, and ground potential is the entrance and the exit of the accelerator. The beams are accelerated toward the terminal by the high voltage of 2.5 MV boosted by Cockroft-Walton type high voltage generator, and a charge of the ions are exchanged to "+3" by stripping the electrons with argon gas stripper

at the terminal and to dissociate background molecules which has the same mass with ^{14}C, such as $^{13}CH^-$ or $^{12}CH_2^-$.

Then $^{12}C^{3+}$, $^{13}C^{3+}$, and $^{14}C^{3+}$ are accelerated toward the exit, and the orbits of each ionized isotope are separated by magnets due to different mass of the isotopes. Finally, abundance of $^{14}C^{3+}$ is counted by a gas ionization detector, whereas currents are measured for $^{12}C^{3+}$ and $^{13}C^{3+}$ by Faraday cups. The ionization detector measures energy-loss rate of the incident ions. Energy-loss rate is proportional to Z^2 (Z: atomic number) (Bethe-Bloch). So, ^{14}C is distinguished from background of isobaric ions by measuring energy-loss rate.

Typically, 28 tree-ring samples, 6 standard samples, and 1 background sample are set in a target wheel, and measured by three runs in one measurement. Each sample is measured for 1600 sec/run. From the one measurement, approximately 200,000 counts of ^{14}C and 100-200 nA of ^{12}C and ^{13}C are obtained for standard samples. Statistical error of the ^{14}C counts is approximately 2.2 ‰. The schematic of the CCR AMS is shown in Figure 3.8 (p 38).

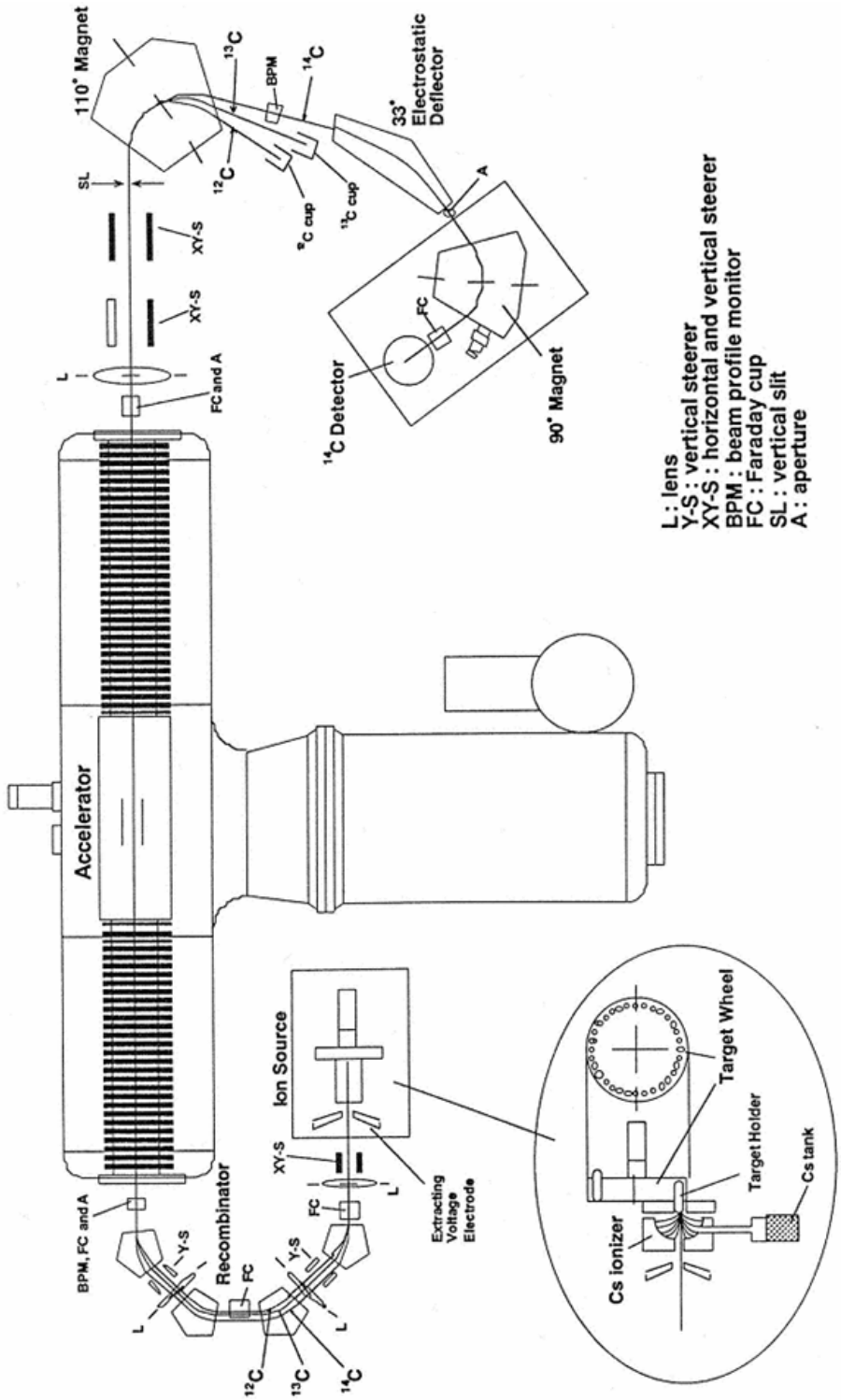

Figure 3.8: The schematic of the AMS at CCR (Nakamura, 2003).

3.4.2 The AMS at MALT, the University of Tokyo

The AMS at MALT is manufactured by NEC (National Electrostatics Corporation), USA. Basic principle of the measurement is the same as the AMS at CCR. However, there are some differences between the AMSs at MALT and CCR. In the AMS at MALT, the C^- beams are injected into the accelerator sequentialy so that each carbon isotope is injected alternately with a period of 0.1 sec. To avoid the overload of the accelerator, proportion of the injection time of the $^{12}C^-$ is smaller than $^{13}C^-$ and $^{14}C^-$. The accelerator of MALT is 5UD Pelletron^{TM} tandem van de Graaf, and the terminal voltage is 5 MV. The exchanged charge of the ions by argon gas stripper at the terminal is "+4".

Typically, 32 tree-ring samples, 6 standard samples, and 1 background sample are set in a target wheel, and measured by five runs in one measurement. Each sample is measured for 300 sec/run. From one measurement, approximately 150,000 counts of ^{14}C and 50-70 μA of ^{12}C and 500-700 nA of ^{13}C are obtained for standard samples. Statistical error of the ^{14}C counts is approximately 2.6 ‰. The schematic of the MALT AMS is shown in Figure 3.9 (p 40).

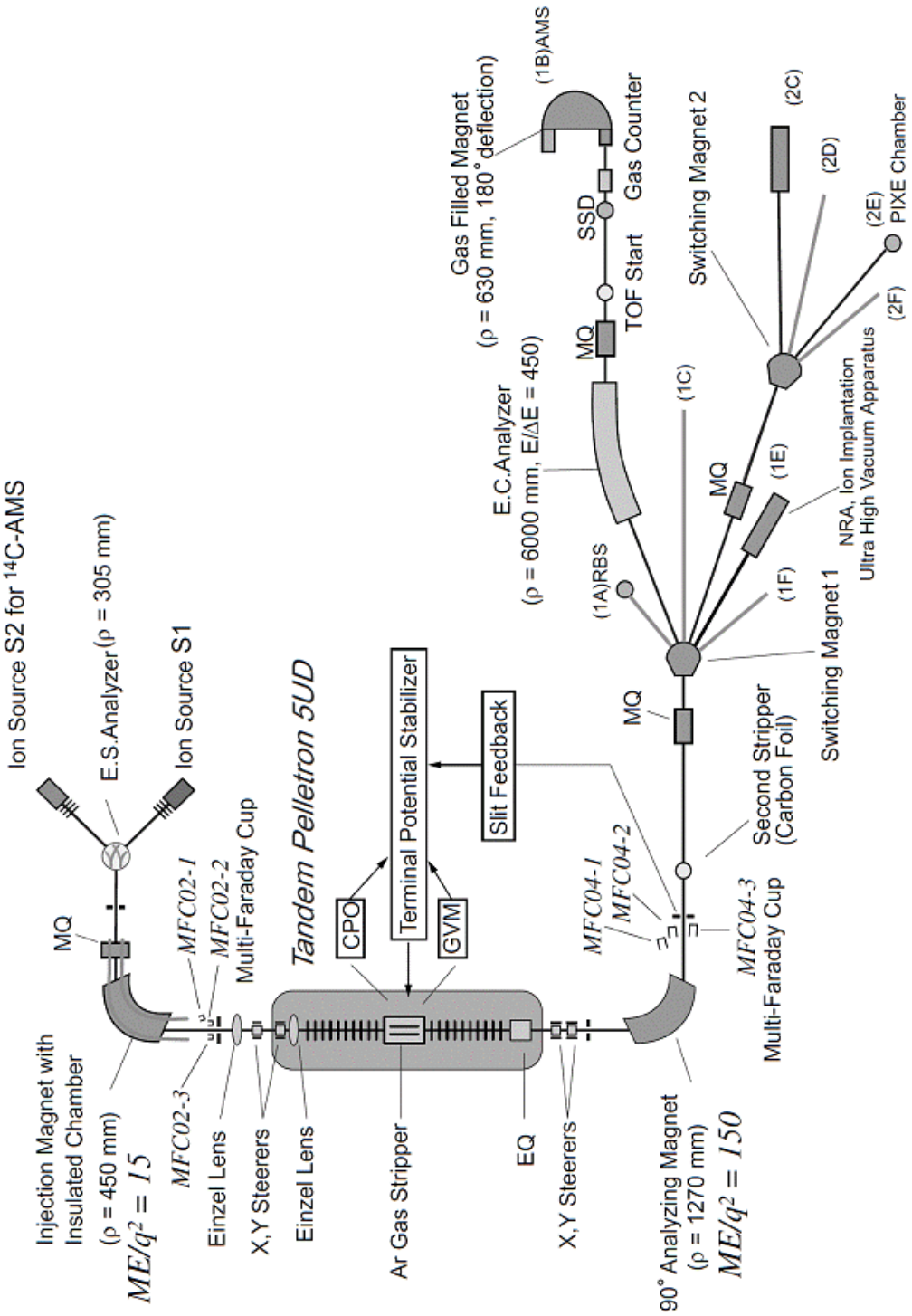

Figure 3.9: The schematic of the AMS at MALT (Matsuzaki et al., 2007).

3.5 Calculations for raw data

Radiocarbon age (carbon-14 age) and Delta C-14 (Δ^{14}C) in the sample tree rings were derived from the measured carbon isotope ratios in graphite targets produced from single-year tree rings. The derivation of carbon-14 age assumes that the atmospheric carbon isotope ratio of carbon-14 to carbon-12 has been constant (Stuiver and Polach, 1977); however, this assumption is not true. Therefore, the carbon-14 age must be converted to the calendar year using the standard calibration curve, IntCal09. On the other hand, atmospheric carbon-14 concentration at the age when the tree ring grew up is calculated as Delta C-14. Delta C-14 expresses a deviation of atmospheric ^{14}C/^{12}C from the "modern value" (Stuiver and Polach, 1977). The value of Delta C-14 is an index of the solar activity variation.

3.5.1 Derivation of radiocarbon age

Radiocarbon age is calculated from the abundance of carbon isotopes measured by using the AMS. Ratio of ^{14}C to ^{12}C, $R14/12$, and ratio of ^{13}C to ^{12}C, $R13/12$ are derived from following equations.

$$R14/12_{spl,std,bkg} = \frac{N_{^{14}C}}{I_{^{12}C} \times t \times D/\left(e \times q\right)}, \tag{3.1}$$

$$R13/12_{spl,std,bkg} = \frac{I_{^{13}C}}{I_{^{12}C} \times D}, \tag{3.2}$$

where the $N_{^{14}C}$ is the total count of ^{14}C, the $I_{^{12}C}$ is the mean current of ^{12}C, the $I_{^{13}C}$ is the mean current of ^{13}C, and the t is the measurement time, with respect to each run. The e is the elementary charge. The subscripts *spl*, *std*, and *bkg* represent the tree-ring sample, the standard sample, and the background sample respectively. The D is the attenuation factor of the $^{12}C^{-}$ current at the recombinator system of CCR AMS as stated in the section 3.4.1. The D is needed only for the data from the CCR, so $D = 90$ for the CCR, and $D = 1$ for the MALT. The q is the charge number of the carbon ions, and $q = 3$ for the CCR, and $q = 4$ for the MALT. Error of the $R14/12_{spl}$ is the statistical one due to the $N_{^{14}C}$, $1/\sqrt{N_{^{14}C}}$. The $R14/12_{std}$ is the weighted average of the 6 standard samples ($R14/12_{std} - i; i = 1 \cdots 6$) by their errors. Each error of the ratio, $R14/12_{std} - i$ is defined as the bigger one of their statistical error or the standard deviation of the $R14/12_{std} - i$. Error of the $R14/12_{std}$ is a combined error of errors of $R14/12_{std} - i$.

The measured isotope ratio is possibly changed from original value in atmosphere due to mass fractionation effect during the photosynthesis, the pretreatment, the target preparation, and the AMS measurement. The ratio $R14/12$ can be corrected by using δ^{13}C, which is the deviation of the stable isotope ratio, $R13/12$ from the reference value. The reference value of δ^{13}C is the $R13/12$ of Pee Dee Belemnite (PDB). The

correction term for $R14/12_{spl,std}$, $Corr_{spl,std}$, is expressed as follows.

$$Corr_{spl,std} = \left(\frac{1 - 25/1000}{1 + \delta^{13}C_{spl,std}/1000} \right)^2 . \tag{3.3}$$

The δ^{13}C is known as -17.8 ‰ for the standard sample, and around -25 ‰ for wood. Here the $\delta^{13}C_{std}$ is the mean value of the 6 standard samples. The $\delta^{13}C_{spl}$ is standardized to the $\delta^{13}C_{std}$ by assuming the average of $\delta^{13}C_{std} - i$ to be -17.8 ‰. The ratio $R14/12_{spl}$ is corrected by the deviation of the standardized $\delta^{13}C_{spl}$ from -25 ‰. The same amount of isotope fractionation effect between ^{13}C and ^{12}C is considered to also affect the ratio between ^{14}C and ^{13}C.

The A_{SN} is obtained by subtracting the background from $R14/12_{spl}$, and multiply the correction factor for the isotope fractionation effect as follows.

$$A_{SN} = (R14/12_{spl} - R14/12_{bkg}) \times Corr_{spl}. \tag{3.4}$$

Relative error of the A_{SN}, E_{SN}, is the same as the relative error of the $R14/12_{spl}$, neglecting the errors of $R14/12_{bkg}$ and $\delta^{13}C_{spl}$.

The reference value of ^{14}C age is determined from the measurement of the standard samples. The $R14/12_{std}$ is corrected by assuming the reference value of the mean $\delta^{13}C_{std}$ to be -17.8 ‰, and multiplied the factor of 0.7459, additionally. Thus the reference value of the carbon-14 age, A_{ON}, is obtained as follows.

$$A_{ON} = 0.7459 \times (R14/12_{std} - R14/12_{bkg}) \times Corr_{std}. \tag{3.5}$$

Relative error of the A_{ON}, E_{ON}, is equal to the relative error of the $R14/12_{std}$.

Conventional radiocarbon age, T, is calculated by using the Libby's half-life, $T_{1/2Libby}$ (5568 years) as follows.

$$T = -T_{1/2Libby}/\ln 2 \times \ln\left(A_{SN}/A_{ON}\right). \tag{3.6}$$

Error of ^{14}C age, E_T is derived from the E_{SN} and the E_{ON} by error propagation as follows.

$$E_T = -T_{1/2Libby}/\ln 2 \times \sqrt{E_{SN}^2 + E_{ON}^2}. \tag{3.7}$$

Finally, carbon-14 ages of the several runs are weighted averaged due to their E_T. Thus the carbon-14 age of each sample is obtained.

3.5.2 Derivation of Delta C-14

The Delta C-14 is the deviation of the age-corrected A_{SN} from the reference value. The reference value of Delta C-14 is the A_{ON} corrected for the age of 1950 AD.

$$\Delta^{14}C = 1000 \times \frac{A_{SN} \times e^{\ln 2/T_{1/2} \times (y-x)} - A_{ON} \times e^{\ln 2/T_{1/2} \times (y-1950)}}{A_{ON} \times e^{\ln 2/T_{1/2} \times (y-1950)}}, \tag{3.8}$$

where y is the year of the AMS measurment, x is the year of the tree ring growth, and $T_{1/2}$ is the half-life of carbon-14 (5730 years) (Godwin,

1962). Error of the Δ^{14}C is derived from the E_{SN} and the E_{ON} by error propagation,

$$E_{\Delta^{14}C} = \left(1000 + \Delta^{14}C\right) \times \sqrt{E_{SN}^2 + E_{ON}^2}. \tag{3.9}$$

3.6 Reproducibility test of the measurement

As a preliminary experiment, a reproducibility test of pretreatment and target preparation was conducted using 9 targets. A tree ring was separated into 9 parts at the wood state. The 9 wood samples were then independently pretreated to prepare 9 targets for measurement using the CCR AMS. The tree-ring sample was obtained from the Japanese cedar tree from Yakushima Island, Japan. The 9 carbon-14 concentrations were in good agreement with a confidence level of more than 95% by the chi-square test ($\chi^2/dof = 1.82$) (Figure 3.10, p 46), which indicates that the systematic error caused by the pretreatment and target preparation system is much smaller than the statistical error. However, in practice, the measured carbon-14 concentration can be influenced to some extent by the status of the AMS system and pretreatment and target preparation systems. Therefore, the reproducibility was monitored by measuring multiple (2-6) targets produced from the same tree ring as stated in the next section.

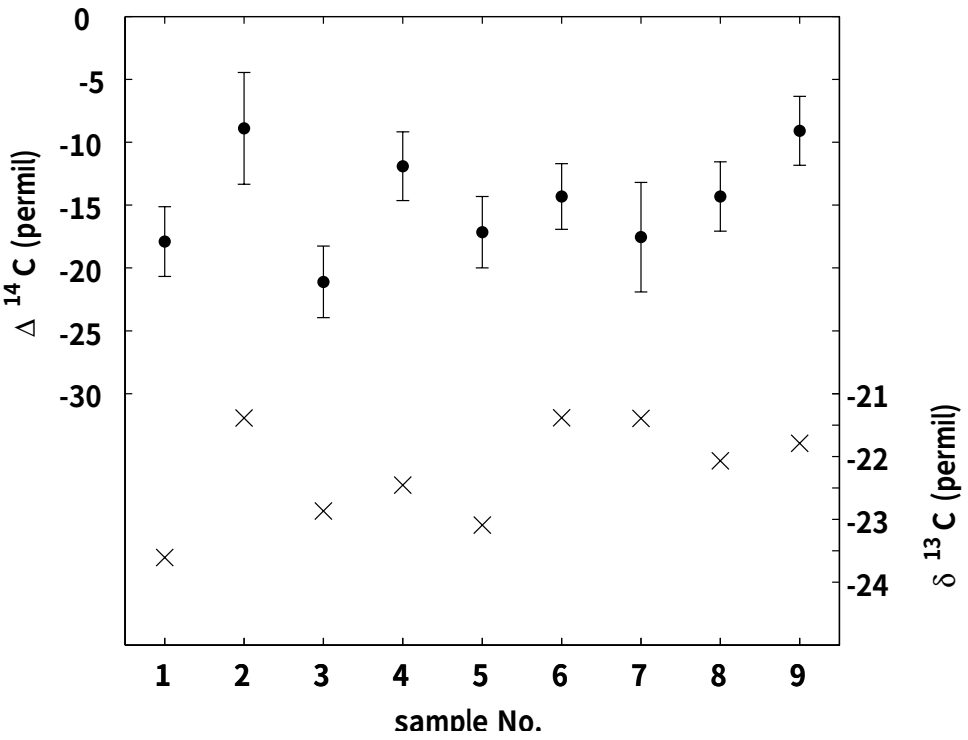

Figure 3.10: The 9 values of Δ^{14}C and δ^{13}C. The 9 samples were independently pretreated and the 9 targets were independently prepared from the samples.

3.7 Pre-dating of the tree rings

To confirm the date of the sample tree, the carbon-14 concentrations in the innermost (oldest) ring, almost the outermost one, and two rings which roughly trisect the whole layers of the tree rings were measured at CCR AMS. The year of the outermost ring was determined to be 149 (+16, −51) BC by using the chi-square test between the 4 carbon-14 ages and standard calibration curve, IntCal. This result is consistent with the previous dating (15 (+154, −90) BC) (Nagaoka et al.,1998) within the

error of 1 σ. Then carbon-14 contents of the biyearly single tree rings from the innermost one to the outer 151st one were measured at the CCR and the MALT. As stated in the section 4.3, the calendar years of these tree rings are 431-281 BC. The period 431-281 BC corresponds to a large peak of the decadal carbon-14 record, as shown in Figure 3.11 (p 47).

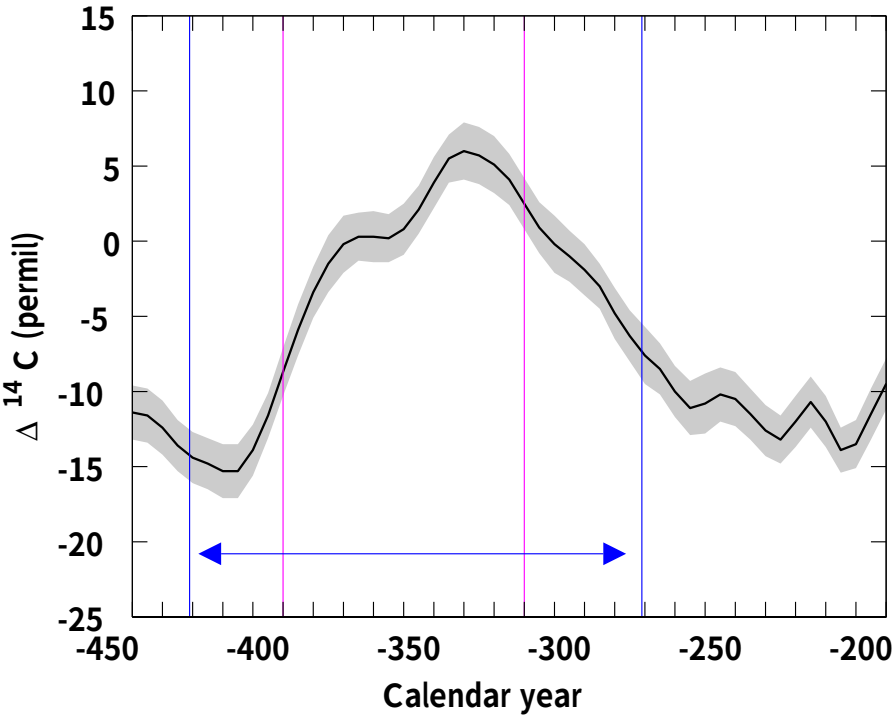

Figure 3.11: IntCal09 curve around 4^{th} century BC (Reimer et al., 2009). The period between the two vertical blue lines was measured in the present study. The period between the two vertical magenta lines represents the estimated prolonged sunspot absence.

Chapter 4

Results

4.1 Data selection

From the bulk samples of cellulose, multiple targets (2-6 targets) were prepared for tree-ring samples of the same year to achieve high precision and to conduct an assessment of the systematic reproducibility. The values of carbon-14 age or Delta C-14 for each tree ring were obtained by averaging with weights based on statistical error, E_T (Section 3.5.1) or $E_{\Delta^{14}C}$ (Section 3.5.2) using criteria (a)-(c) listed below, which were introduced to exclude poorly-reproducible results beyond the statistical errors. The weight of the i-th value ($i = 1 \cdots n$; n = 2-6) of each tree ring, W_i, is defined as

$$W_i = \frac{E_i^{-2}}{\sum_{i=1}^{n} E_i^{-2}}. \tag{4.1}$$

The weighted average of X_i ($X =^{14}$C age, T or Δ^{14}C, C), X_m, is defined as

$$X_m = \sum_{i=1}^{n} \left(X_i \times W_i \right). \tag{4.2}$$

The reduced chi-square of X is defined as

$$\chi^2/dof = \frac{1}{n-1} \times \sum_{i=1}^{n} \left(\frac{X_m - X_i}{E_i} \right)^2. \tag{4.3}$$

Delta C-14 data of 76 tree rings were obtained in the present study (biennially during 431-281 BC). The ratio, 1/76 is equal to 1.3%, so that the rejection rate was estimated to be smaller than approximately 99% from chi-square test, which is permissible. A rejection rate smaller than 99% corresponds to a reduced chi-square smaller than approximately 4. Hence, criterion-(a): if the reduced chi-square, χ^2/dof of the X_i is smaller than 4, all data (i = 1-n) are used for averaging and the resultant error is applied. The resultant value, X_r and the resultant error, E_r are defined as

$$X_r = X_m, \tag{4.4}$$

and

$$E_r = \frac{1}{\sqrt{\sum_{i=1}^{n} E_i^{-2}}}. \tag{4.5}$$

Criterion-(b): if the reduced chi-square is larger than 4, the most outlier was excluded from the averaging (from the calculation of W_i, X_m, and

χ^2/dof, and this procedure is repeated until the improved reduced chi-square becomes less than 4 and the X_r and E_r were also improved. Criterion-(c): in the case where the nearest 2 data of 2-6 data do not satisfy the criterion $\chi^2/dof < 4$, then the 2 data are averaged and the standard deviation of those data is adopted to the E_r as

$$E_r = \sqrt{\frac{1}{2} \times \sum_{i=1}^{2} (X_m - X_i)^2}. \tag{4.6}$$

4.2 Data I - Radiocarbon age

Resultant radiocarbon age and error, T_r and E_r from each tree ring are listed in the Table 4.1.

Table 4.1: Resultant radiocarbon ages and their error. The first column shows the tree-ring number (No.1 corresponds to the oldest ring), the second column shows the resultant radiocarbon ages, T_r in years BP, and the third column shows their resultant error, E_r. Years BP represents the past years from 1950 AD.

Tree-ring No.	T_r (years BP)	E_r (years)
1	2454.0	82.1
3	2435.2	20.6
5	2417.0	21.1
7	2419.3	22.2
9	2501.0	22.7
11	2480.3	23.9
13	2475.7	22.9

Table 4.1: Resultant radiocarbon ages and their error. The first column shows the tree-ring number (No.1 corresponds to the oldest ring), the second column shows the resultant radiocarbon ages, T_r in years BP, and the third column shows their resultant error, E_r. Years BP represents the past years from 1950 AD.

Tree-ring No.	T_r (years BP)	E_r (years)
15	2432.0	23.7
17	2409.8	86.8
19	2344.6	86.8
21	2388.2	21.4
23	2477.0	21.9
25	2398.2	22.0
27	2374.6	23.5
29	2386.6	15.3
31	2350.4	15.5
33	2364.6	16.4
35	2347.5	16.4
37	2300.3	16.9
39	2314.0	16.6
41	2313.8	16.6
43	2330.1	17.9
45	2348.3	16.6
47	2314.2	17.1
49	2306.4	16.5
51	2293.0	17.2
53	2296.8	17.3
55	2352.4	17.6
57	2297.0	13.3
59	2271.8	12.9
61	2256.2	18.0
63	2273.8	15.3

Table 4.1: Resultant radiocarbon ages and their error. The first column shows the tree-ring number (No.1 corresponds to the oldest ring), the second column shows the resultant radiocarbon ages, T_r in years BP, and the third column shows their resultant error, E_r. Years BP represents the past years from 1950 AD.

Tree-ring No.	T_r (years BP)	E_r (years)
65	2193.8	21.2
67	2258.0	18.9
69	2203.7	16.3
71	2241.4	18.1
73	2244.8	15.8
75	2229.8	17.4
77	2217.6	16.7
79	2186.5	16.6
81	2216.2	17.1
83	2170.4	15.7
85	2219.1	16.6
87	2225.1	13.3
89	2163.7	12.8
91	2267.4	88.2
93	2216.1	15.0
95	2168.0	17.3
97	2150.0	16.8
99	2194.1	17.1
101	2123.6	19.4
103	2250.5	17.5
105	2186.9	17.4
107	2173.7	19.5
109	2168.3	15.7
111	2212.1	18.9
113	2216.5	16.0

Table 4.1: Resultant radiocarbon ages and their error. The first column shows the tree-ring number (No.1 corresponds to the oldest ring), the second column shows the resultant radiocarbon ages, T_r in years BP, and the third column shows their resultant error, E_r. Years BP represents the past years from 1950 AD.

Tree-ring No.	T_r (years BP)	E_r (years)
115	2271.1	16.2
117	2215.6	18.1
119	2242.6	64.4
121	2255.3	19.3
123	2256.9	21.5
125	2203.2	19.0
127	2235.4	70.2
129	2206.1	19.9
131	2239.4	19.1
133	2223.8	19.3
135	2286.8	21.1
137	2210.2	65.8
139	2214.9	18.9
141	2285.8	18.4
143	2194.5	18.5
145	2265.5	19.0
147	2263.3	18.0
149	2210.9	61.7
151	2288.8	80.6

4.3 Radiocarbon dating of the tree rings

The radiocarbon age (carbon-14 age) of the sample tree was derived from the measured carbon isotope ratios in graphite targets produced from single-year tree rings. The derivation of carbon-14 age assumes that the atmospheric carbon isotope ratio of carbon-14 to carbon-12 has been constant (Stuiver and Polach, 1977). However, this assumption is not true. Therefore, the carbon-14 age must be converted to the calendar year using the standard calibration curve, IntCal09. This can be achieved using the calibration program, Oxcal (Bronk Ramsey et al., 2001), which calculates the probability distribution of the calendar year for a carbon-14 data set using a maximum-likelihood method. The relative ages of the tree rings are fixed by the counted number of tree rings. Therefore, the D_Sequence function (Bronk Ramsey, 2008) in Oxcal was used. The calendar year of the outermost (youngest) tree ring (No. 151 in Table 4.1) is estimated as 278-283 BC (the maximum probability is 281 BC) with a confidence level of 95%. This means that the data covers the period of 431-281 BC corresponding to the large peak of the decadal carbon-14 record, as represented by black mark on the x-axis in Figure 3.11 (p 47).

4.4 Data II - Delta C-14

The atmospheric carbon-14 concentrations in the ages when the tree rings grew were calculated. C_i (as stated in the Section 3.5.1) of each year determined in the Section 4.3 are listed in the Table 4.2.

Table 4.2: Calculated 2-6 values of Δ^{14}C of each year. The 1st column shows the tree-ring calendar age, the 2-7th columns show the individual results of Δ^{14}C, C_i (‰) for i-th samples (i = 1-6), the 8-13th columns show the each error, E_i (‰), and the 14th and 15th columns show the χ^2/dof before and after data selection respectively. The red figures represent the excluded values according to the criteria (Section 4.1) and the improved χ^2/dof by the data selection.

Year	C_1	C_2	C_3	C_4	C_5	C_6	E_1	E_2	E_3	E_4	E_5	E_6	χ^2/dof	χ^2/dof
-431	-10.4	-24.6					3.4	3.7					8.1	1.0
-429	-16.9	-12.5					3.4	3.7					0.7	0.7
-427	-15.0	-10.5					3.5	3.8					0.7	0.7
-425	-16.4	-8.9					3.5	4.3					1.8	1.8
-423	-26.9	-21.0					4.1	3.7					1.1	1.1
-421	-19.4	-23.4					4.1	4.2					0.5	0.5
-419	-21.1	-21.0					4.2	3.7					0.0	0.0
-417	-21.7	-12.2					4.6	3.7					2.6	2.6
-415	-20.5	-5.4					4.1	4.4					6.4	1.0
-413	-14.0	1.2					4.5	4.1					6.2	1.0
-411	-14.3	-8.0					3.7	3.8					1.5	1.5
-409	-20.9	-23.7					3.9	3.7					0.3	0.3
-407	-9.6	-16.1					3.9	3.7					1.5	1.5
-405	-10.2	-10.4					4.0	4.2					0.0	0.0
-403	-16.4	-10.2	-13.5	-9.6			4.5	3.4	3.6	3.8			0.6	0.6
-401	-4.4	-11.1	-8.1	-6.7			3.9	3.6	3.6	4.4			0.6	0.6
-399	-4.3	-15.9	-7.8				3.9	3.4	3.3				2.8	2.8
-397	-9.1	-8.6	-6.2				4.0	3.2	3.5				0.2	0.2
-395	-9.2	1.0	0.0				3.9	3.5	3.6				2.2	2.2
-393	-4.2	-10.6	0.9				3.9	3.6	3.3				2.8	2.8

Table 4.2: Calculated 2-6 values of Δ^{14}C of each year. The 1st column shows the tree-ring calendar age, the 2-7th columns show the individual results of Δ^{14}C, C_i (‰) for i-th samples (i = 1-6), the 8-13th columns show the each error, E_i (‰), and the 14th and 15th columns show the χ^2/dof before and after data selection respectively. The red figures represent the excluded values according to the criteria (Section 4.1) and the improved χ^2/dof by the data selection.

Year	C_1	C_2	C_3	C_4	C_5	C_6	E_1	E_2	E_3	E_4	E_5	E_6	χ^2/dof	χ^2/dof
-391	-6.2	-4.8	-2.8				3.9	3.4	3.4				0.2	0.2
-389	-5.9	-6.7	-7.5				4.0	3.6	3.9				0.0	0.0
-387	-8.9	-11.5	-7.0				4.0	3.3	3.5				0.4	0.4
-385	-12.0	-1.5	-4.0				4.1	3.5	3.5				2.0	2.0
-383	-6.3	-5.0	-2.6				3.9	3.3	3.5				0.3	0.3
-381	-2.1	-4.9	-2.3				3.8	3.7	3.6				0.2	0.2
-379	-0.2	-6.1	-4.6				4.0	3.7	3.5				0.6	0.6
-377	-4.9	-15.4	-11.5				3.9	3.6	3.8				2.0	2.0
-375	-2.3	-2.6	-9.5	-8.6	4.8	5.0	4.4	3.6	3.7	3.2	3.4	4.0	3.1	3.1
-373	2.3	-4.8	-4.9	0.3	-0.2		4.2	3.6	3.9	3.3	3.2		0.7	0.7
-371	1.3	-0.8					3.2	3.2					0.2	0.2
-369	1.0	-6.6	-0.2				3.6	3.2	3.2				1.5	1.5
-367	5.9	10.5					3.3	4.4					0.7	0.7
-365	1.3	-2.5					3.4	3.2					0.7	0.7
-363	12.1	4.4	3.7				4.3	3.2	3.3				1.4	1.4
-361	0.8	2.3	-1.1				5.5	3.2	3.8				0.2	0.2
-359	11.6	-1.7	-3.9				4.3	3.2	3.1				4.6	1.5
-357	6.2	0.6	1.4				5.3	3.2	3.5				0.4	0.4
-355	6.0	1.1	3.6				4.5	3.3	3.4				0.4	0.4
-353	9.1	10.3	2.0				4.3	3.4	3.3				1.7	1.7
-351	3.2	3.4	1.4				3.5	3.4	4.4				0.1	0.1
-349	10.1	10.6	4.4				3.5	3.3	3.4				1.1	1.1
-347	8.1	-2.3	7.0	20.0	-12.4		4.5	3.3	3.3	3.4	3.4		12.7	2.9
-345	4.9	-0.1	8.2	-1.4	-4.1		5.6	3.3	3.6	3.3	3.8		1.7	1.7
-343	0.1	6.8	10.5	11.5	12.3		3.8	3.5	3.4	3.4	3.9		1.8	1.8
-341	7.1	-3.5	-14.7				4.4	3.3	3.7				7.5	0.3
-339	4.3	6.0	-4.0	-0.5			4.3	3.3	3.4	4.4			1.7	1.7
-337	9.1	6.0	7.4				5.2	3.4	3.3				0.1	0.1
-335	12.7	8.6	7.5				4.3	3.5	3.4				0.5	0.5

Table 4.2: Calculated 2-6 values of Δ^{14}C of each year. The 1st column shows the tree-ring calendar age, the 2-7th columns show the individual results of Δ^{14}C, C_i (‰) for i-th samples (i = 1-6), the 8-13th columns show the each error, E_i (‰), and the 14th and 15th columns show the χ^2/dof before and after data selection respectively. The red figures represent the excluded values according to the criteria (Section 4.1) and the improved χ^2/dof by the data selection.

Year	C_1	C_2	C_3	C_4	C_5	C_6	E_1	E_2	E_3	E_4	E_5	E_6	χ^2/dof	χ^2/dof
-333	3.8	2.2	4.3				4.5	3.4	3.4				0.1	0.1
-331	7.5	16.0	8.3				5.6	3.5	4.4				1.4	1.4
-329	-1.4	-2.4	-6.8				5.4	3.4	3.3				0.6	0.6
-327	1.2	10.0	-1.9				5.6	3.4	3.3				3.3	3.3
-325	-2.9	7.4	6.6				5.3	3.5	4.5				1.4	1.4
-323	3.3	4.0	8.9				3.3	3.5	3.4				0.8	0.8
-321	-14.4	0.9	-1.8				3.6	3.3	3.3				5.5	3.7
-319	-7.0	1.3	4.9				3.2	3.3	4.0				3.1	3.1
-317	-4.3	-12.4	-6.6				3.2	3.1	4.3				1.7	1.7
-315	-2.8	-0.2					3.2	3.2					0.3	0.3
-313	1.2	-10.1					3.6	3.2					5.6	0.5
-311	-2.6	-10.3					3.6	3.2					2.6	2.6
-309	-1.4	-10.2					4.6	3.2					2.4	2.4
-307	-2.8	0.7					3.6	3.2					0.5	0.5
-305	1.7	-10.6					3.6	3.2					6.6	1.0
-303	-6.2	2.1					3.7	3.3					2.8	2.8
-301	-5.7	-6.4					3.6	3.1					0.0	0.0
-299	-7.0	-2.6					3.7	3.1					0.8	0.8
-297	-9.8	-13.8					4.4	3.2					0.5	0.5
-295	-9.8	1.8					3.6	3.1					5.9	1.0
-293	-1.5	-6.1					3.5	3.2					1.0	1.0
-291	-10.1	-16.2					3.1	3.3					1.8	1.8
-289	-5.1	1.7					3.1	3.4					2.2	2.2
-287	-9.1	-13.3					3.2	3.5					0.8	0.8
-285	-6.6	-15.5					3.1	3.2					4.0	1.0
-283	0.2	-10.6					3.2	3.5					5.3	1.0
-281	-21.6	-7.6					3.4	3.4					8.7	1.0

The 4 C_i out of 207 C_i were excluded due to the data selection (the criterion-(b)). The excluded 4 $C_i(t)$ (t is the ages) correspond to the 3 ages, that are -359, -347, and -321. The ages corresponding to the χ^2/dof which is improved by the error extension (the criterion-(c)) are -431, -415, -413, -341, -305, -295, -285, -283, and -281. The values of C_i and χ^2/dof in Table 4.2 are plotted in Figure 4.1 (p 62). Resultant Δ^{14}C values, C_r in each year are listed in Table 4.3 and plotted in Figure 4.1. The data of 53 ages out of 76 ages were taken at both CCR and MALT AMS facilities. The two data sets from the different AMS facilities were in good agreement with each other ($\chi^2/dof = 1.26$). The present result is compared with the IntCal in Figure 4.2 (p 63). The data fluctuate from IntCal09, which is estimated from the decadal Delta C-14 change. This fluctuation is considered to be due to the solar Schwabe cycle and systematic uncertainty. The difference from one C_r data to the next is occasionally too large to be due to a change in carbon-14 production; therefore, systematic noise was assumed to be included after carbon-14 production. For example, systematic uncertainty may be due to the climatic change of the sample tree growing environment. However, such large differences rarely occur and are non-periodical; therefore, it does not affect the signal of the Schwabe cycle in the Δ^{14}C record, C_r.

Table 4.3: The present Delta C-14 record and error. The first column shows the calendar year, the second column shows the resultant Δ^{14}C data, C_r, and the third column shows the resultant error, E_r.

Year	C_r (‰)	E_r (‰)
-431	-16.96	10.04
-429	-14.89	2.52
-427	-12.90	2.59
-425	-13.42	2.73
-423	-23.64	2.76
-421	-21.35	2.91
-419	-21.04	2.79
-417	-15.93	2.90
-415	-13.44	10.66
-413	-5.65	10.75
-411	-11.26	2.63
-409	-22.37	2.67
-407	-12.98	2.70
-405	-10.31	2.90
-403	-12.03	1.89
-401	-7.81	1.92
-399	-9.80	2.02
-397	-7.93	2.03
-395	-2.32	2.10
-393	-4.26	2.06
-391	-4.48	2.05
-389	-6.74	2.21
-387	-9.23	2.05
-385	-5.25	2.12
-383	-4.53	2.05
-381	-3.10	2.14
-379	-3.82	2.14
-377	-10.93	2.17

Table 4.3: The present Delta C-14 record and error. The first column shows the calendar year, the second column shows the resultant Δ^{14}C data, C_r, and the third column shows the resultant error, E_r.

Year	C_r (‰)	E_r (‰)
-375	-2.59	1.49
-373	-1.44	1.60
-371	0.27	2.25
-369	-2.16	1.91
-367	7.57	2.66
-365	-0.69	2.35
-363	5.85	2.04
-361	0.90	2.25
-359	-2.84	1.97
-357	1.86	2.17
-355	3.13	2.09
-353	6.78	2.08
-351	2.83	2.14
-349	8.31	1.97
-347	3.46	2.07
-345	0.99	1.66
-343	8.42	1.60
-341	-4.75	10.93
-339	1.39	1.87
-337	7.16	2.17
-335	9.17	2.11
-333	3.41	2.13
-331	12.00	2.44
-329	-4.10	2.16
-327	3.57	2.18
-325	4.98	2.44
-323	5.41	1.96
-321	-0.42	2.35

Table 4.3: The present Delta C-14 record and error. The first column shows the calendar year, the second column shows the resultant Δ^{14}C data, C_r, and the third column shows the resultant error, E_r.

Year	C_r (‰)	E_r (‰)
-319	-1.09	1.99
-317	-8.10	2.00
-315	-1.46	2.25
-313	-5.05	7.98
-311	-6.87	2.39
-309	-7.30	2.65
-307	-0.88	2.37
-305	-5.13	8.69
-303	-1.72	2.47
-301	-6.10	2.36
-299	-4.40	2.39
-297	-12.42	2.60
-295	-3.20	8.17
-293	-4.03	2.35
-291	-13.01	2.26
-289	-1.98	2.29
-287	-10.99	2.34
-285	-10.97	6.29
-283	-4.74	7.65
-281	-14.58	9.89

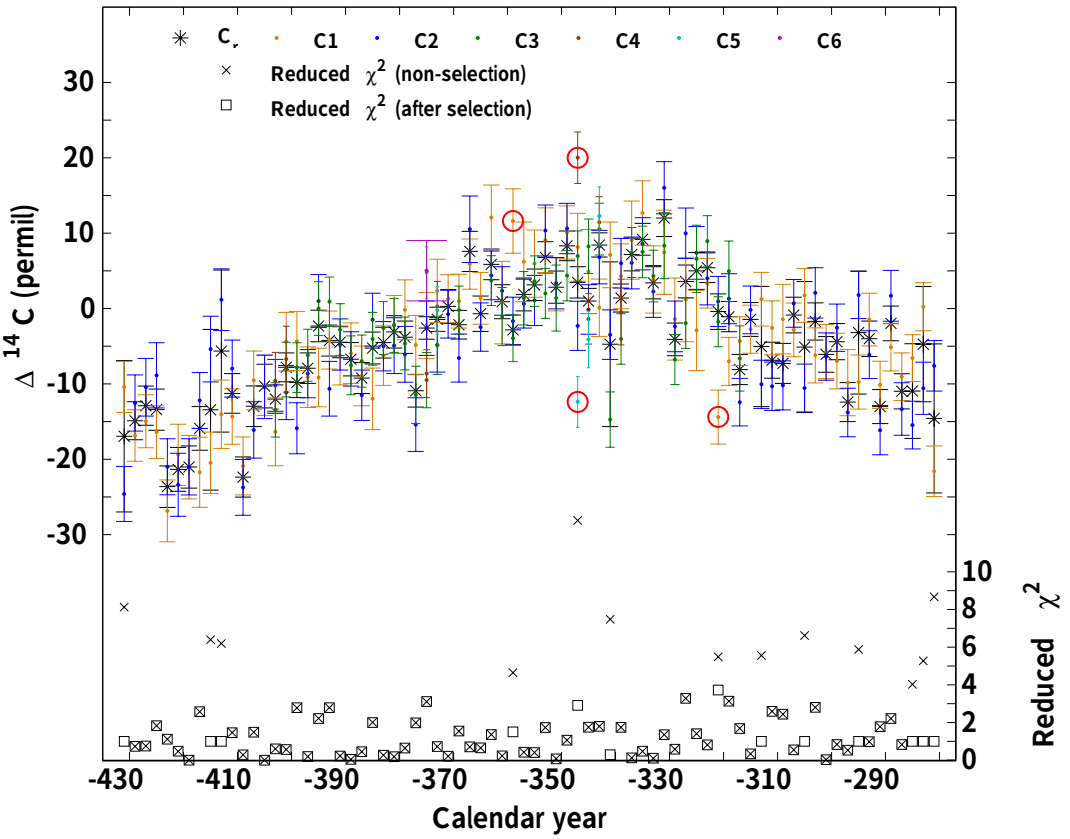

Figure 4.1: The x-axis represents the calendar year and the y-axis (left hand) represents Δ^{14}C in ‰. The y-axis (right hand) represents reduced chi-square. The six-color dots and error bars represent the results of the individual measuremnt (C_i), the red circle represent the excluded data by selection, asterisks and error bars represent the resultant Δ^{14}C value, C_r. The squares and crosses represent the χ^2/dof before and after the data selection.

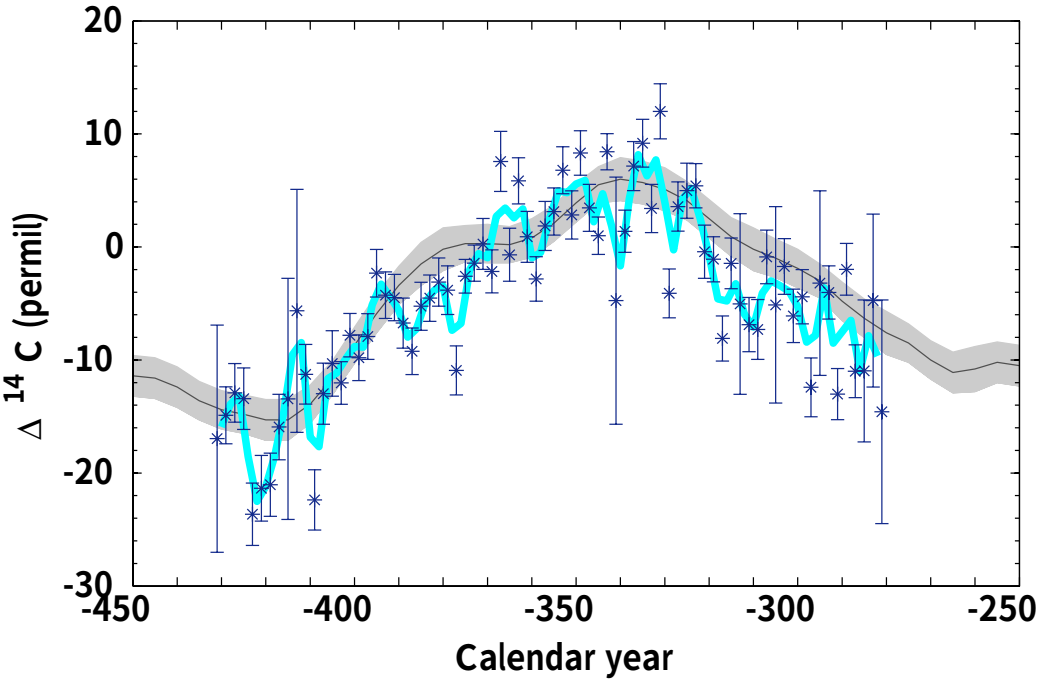

Figure 4.2: The x-axis and y-axis are the same with Figure 4.1 (p 62). The gray curve and area represent the IntCal data and error, navy dots and error bars represent the C_r, and the blue curve represents the 3-year running average of the C_r.

4.5 Periodicity analysis

To obtain a frequency spectrum of the temporal variation of Δ^{14}C due to the Schwabe cycle, the time series of Δ^{14}C was analyzed using the S-transform (Stockwell et al., 1996; Pinnegar and Mansinha, 2004), which is a wavelet transform. The wavelet transform transforms the observed time series of Δ^{14}C into power spectrum or amplitude spectrum on a space of time and frequency. As a mother wavelet function, the S-transform uses the product of a sinusoidal function and a Gaussian func-

tion of which the variance is equal to $1/f^2$ (where f is the frequency of the sinusoidal function). The mother wavelet $w(t, f)$ is given as

$$w(t, f) = \frac{|f|}{\sqrt{2\pi}} e^{-\frac{t^2 f^2}{2}} e^{-i2\pi ft}. \tag{4.7}$$

This mother wavelet is a basis function, and it transforms the original time series $C_r(t)$ into a time-local frequency spectrum $S(\tau, f)$ which shows how the amplitude and phase change over time τ. The S can be converted into a power spectrum P or an amplitude spectrum A on a space of time and frequency as follows.

$$S_{C_r}(\tau, f) = \int_{-\infty}^{\infty} C_r(t) \frac{|f|}{\sqrt{2\pi}} e^{-\frac{(\tau - t)^2 f^2}{2}} e^{-i2\pi ft} dt, \tag{4.8}$$

$$A_{C_r}(\tau, f) = |S_{C_r}(\tau, f)|, \tag{4.9}$$

$$P_{C_r}(\tau, f) = |S_{C_r}(\tau, f)|^2. \tag{4.10}$$

The result of the S-transform for the present Δ^{14}C record (C_r) is shown in Figure 4.3 (p 65) and Figure 4.4 (p 65), where the color scale represents $A(\tau, f)$ (‰) or $P(\tau, f)$ (‰^{2}), which is the amplitude and power spectrum of each frequency component at each time in the Δ^{14}C record. The amplitudes enhancement of 1-2 ‰ around $f \sim 0.1$ year^{-1} at 431-380 BC, $f \sim 0.07$ year^{-1} at 380-340 BC, and $f \sim 0.1$ year^{-1} at 340-281 BC can be due to the Schwabe cycle. The low-frequency components ($f \geq 0.025$) are due to the long-term increase of Δ^{14}C during the grand solar minimum.

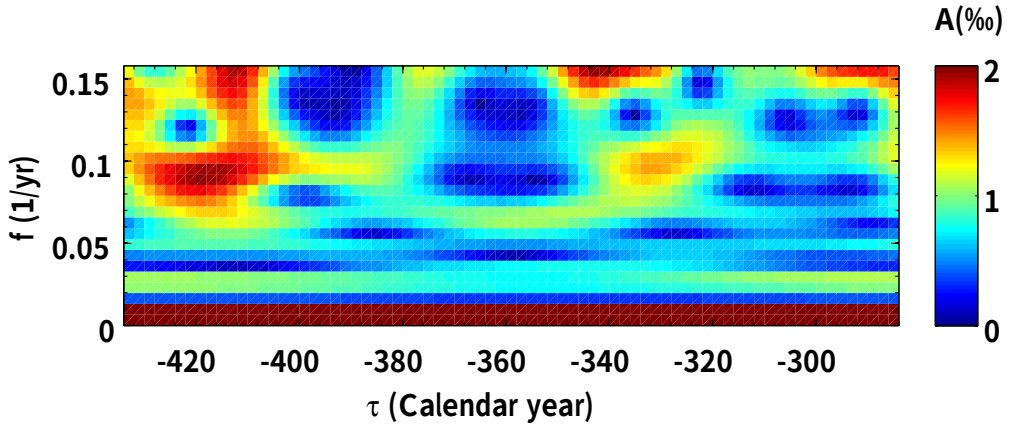

Figure 4.3: The result of the S-transform for the present Δ^{14}C data (C_r). The x-axis represents τ (calendar year), the y-axis represents f (year^{-1}), and the color scale represents $A(\tau, f)$ (‰).

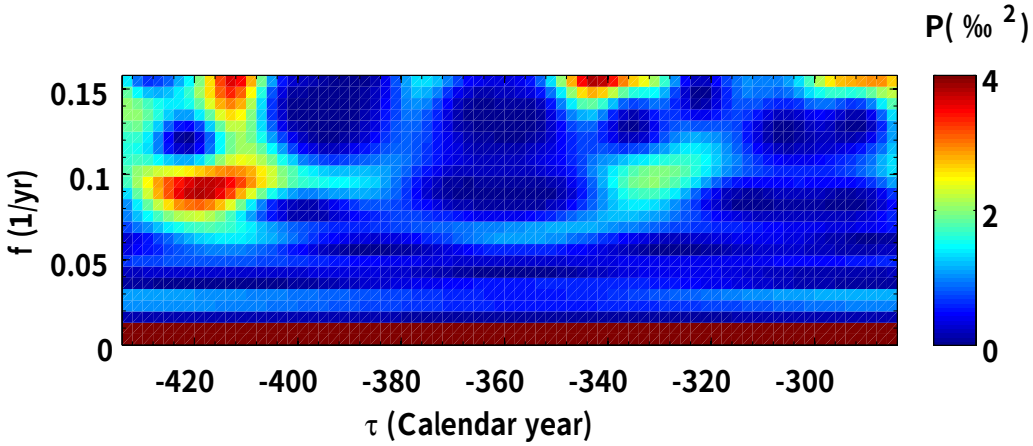

Figure 4.4: The x-axis and the y-axis are the same as those in Figure 4.3 (p 65), but the color scale represents $P(\tau, f)$ (‰^{2}).

4.6 Confidence level of the Schwabe cycle signals

The confidence level of the amplitude (or power) spectrum was assessed using a Monte Carlo simulation. The S-transform is a linear operation; therefore, the power spectrum for the original time series, $C_r(t) = signal + noise$ can be expressed as

$$S_{C_r(t)} = S_{signal} + S_{noise}. \tag{4.11}$$

The probability density distribution of the power spectrum derived only from noise (distribution of S_{noise}) is simulated. If the present Δ^{14}C record contains some signals ($S_{signal} > 0$), then the probability that S_{noise} exceeds $S_{C_r(t)}$ should be low. The simulation procedure are outlined as follows. Normally distributed random variables (average=0) of the same number as that of the Δ^{14}C data set (=76) are generated. Here, each standard deviation of the normal distributions is equal to the errors of each Δ^{14}C data (E_r) (Figure 4.5 (a), p 68). Random variables are considered as the simulated Δ^{14}C record, which contains only noise without signals and is converted into a power spectrum using the S-transform (Figure 4.5 (b), p 68). Thus, the S_{noise} for each τ and f are obtained. These procedures are repeated 10000 times, and the probability density distribution of $P_{noise}(\tau, f)$ is obtained. The $P_{noise}(\tau, f)$ is always positive (Equation 4.10), and the probability density distribution of $P_{noise}(\tau, f)$ is

exponentially downward-sloping. The probability density distribution of $P_{noise}(\tau, f)$ is fitted using an exponential distribution and the parameter μ is determined for each τ and f (Figure 4.5 (c), p 68).

$$D_{exp}(x) = \frac{1}{\mu} e^{\frac{-x}{\mu}}. \tag{4.12}$$

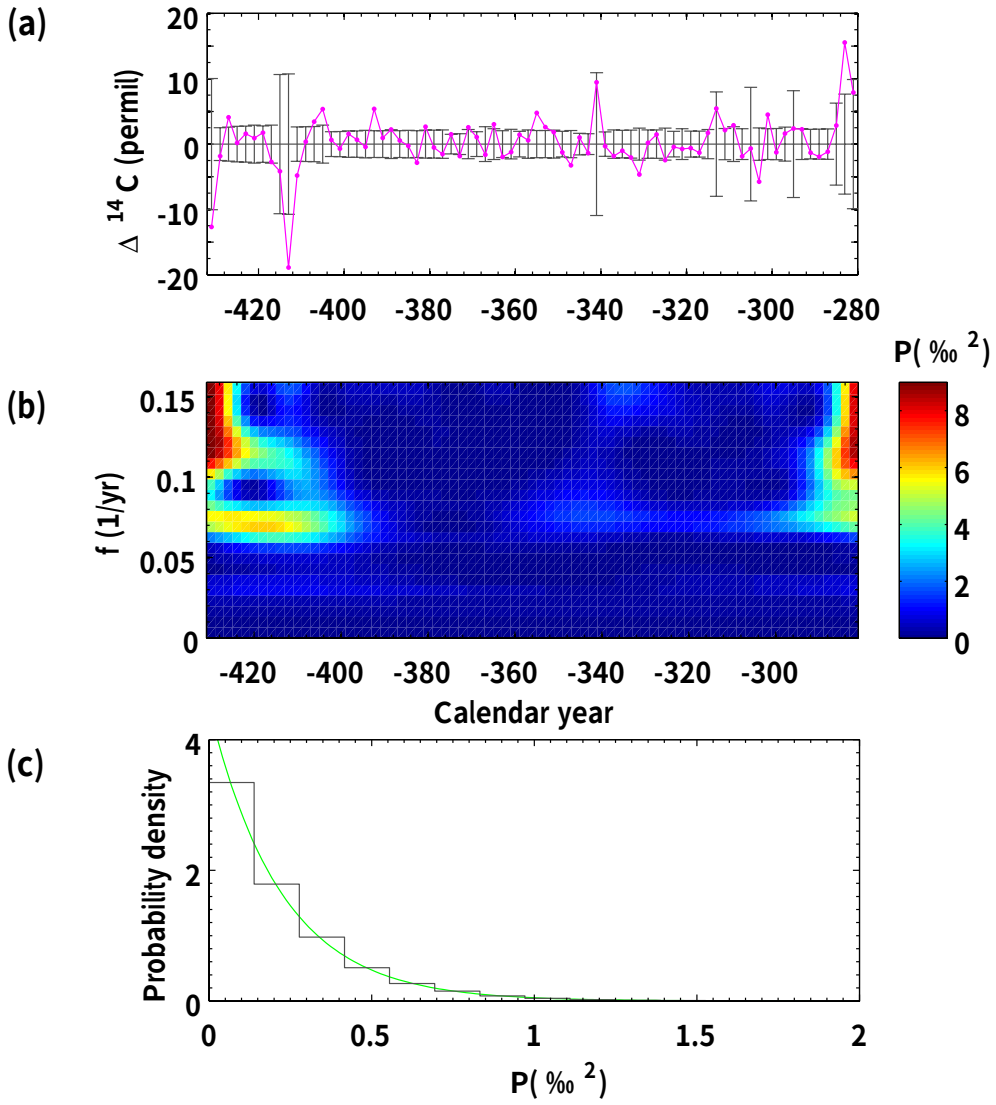

Figure 4.5: (a) An example of the simulated Δ^{14}C record (pink dots and line) out of 10,000 times simulation. The error bars represent the standard deviation of normal distributions, which is equal to the errors of Δ^{14}C record, C_r. (b) The power spectrum by S-transform for the simulated Δ^{14}C record example, (a). (c) An example of the histogram of the P_{noise} from the 10,000 simulations at $(\tau, f) = (-377, 0.092)$. The stairs represent the histogram which is obtained from simulation, and the green curve represents the fitting curve of exponential distribution (Equation 4.12) for the histogram.

In exponential distribution (Equation 4.12, p 67), the expected value and the standard deviation are μ. The distribution of $\mu(\tau, f)$ obtained by the Monte Carlo simulation is represented in Figure 4.6 (p 69). On the lines of the constant τ, the $\mu(\tau, f)$ depend on the f. High-frequency power spectrum is easier to be produced than low-frequency power spectrum by random noise. The τ of large $\mu(\tau, f)$ correspond to that of large $E_r(\tau)$ on the lines of the constant f. $\mu(\tau, f)$ is dependent on the errors of the Δ^{14}C data around τ.

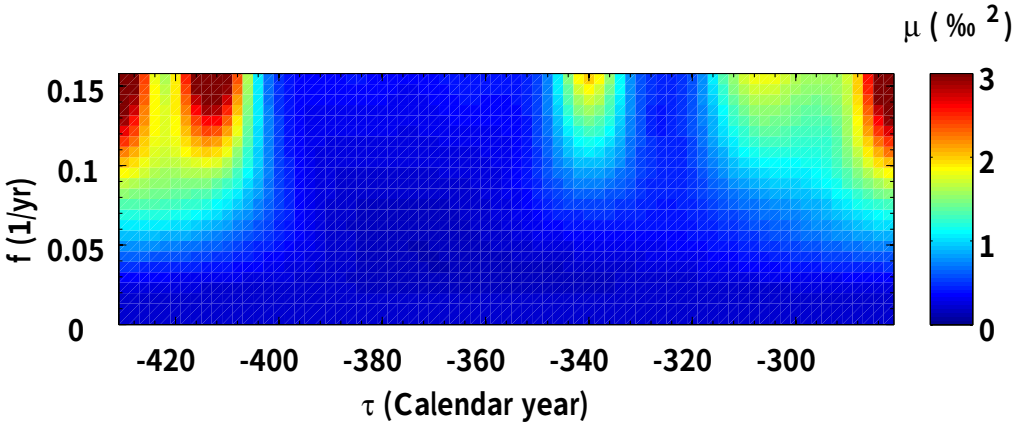

Figure 4.6: The x-axis and the y-axis are the same as those in Figure 4.3 (p 65), but the color scale represents $\mu(\tau, f)$.

The confidence level $CL(\tau, f)$ and significance $\sigma(\tau, f)$ is defined as follows.

$$CL(\tau, f) = \int_0^{P_{C_r(t)}(\tau,f)} D_{exp}(x; \mu(\tau, f))dx, \tag{4.13}$$

$$\sigma(\tau, f) = \frac{P_{C_r(t)}(\tau, f)}{\mu(\tau, f)}. \tag{4.14}$$

The distribution of $CL(\tau, f)$ is represented in Figure 4.7 (p 70), and the

distribution of $\sigma(\tau, f)$ is represented in Figure 4.8 (p 71). I consider a confidence level of more than 95% as a significant signal. $CL(\tau, f) \geq 0.95$ corresponds to $\sigma(\tau, f) \geq 3$ in the exponential distribution. The three regions of (τ, f) space give significant signals; the first, $f \sim 0.092$ year^{-1} ($\sim 1/11$ year^{-1}), $\tau \sim 406 - 380$ BC; the second, $f \sim 0.066$ year^{-1} ($\sim 1/15$ year^{-1}), $\tau \sim 390 - 352$ BC; and the third, $f \sim 0.092$ year^{-1} ($\sim 1/11$ year^{-1}), $\tau \sim 336 - 324$ BC. The 3 σ is indicated by white lines in Figure 4.7 and 4.8, which are sufficiently separated from the noise components and seem to be derived from the Schwabe cycle with respect to their cycle length.

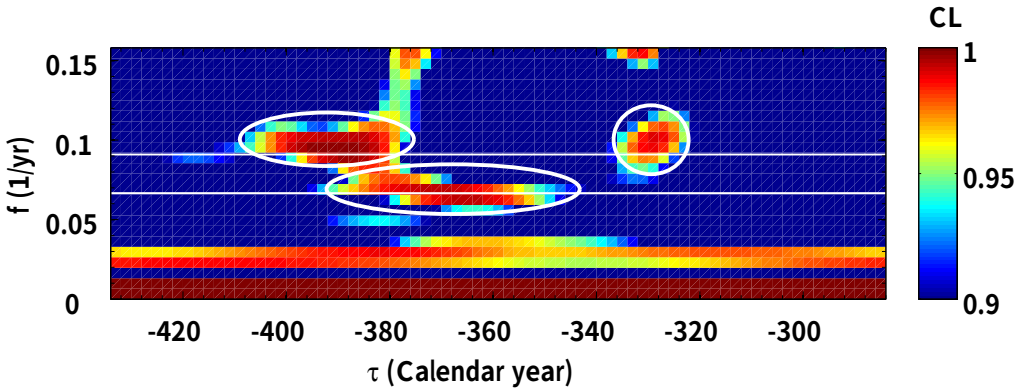

Figure 4.7: The x-axis and the y-axis are the same as those in Figure 4.3 (p 65), but the color scale represents $CL(\tau, f)$. The two white horizontal lines represent $f = 1/11$ and $f = 1/15$ (1/yr).

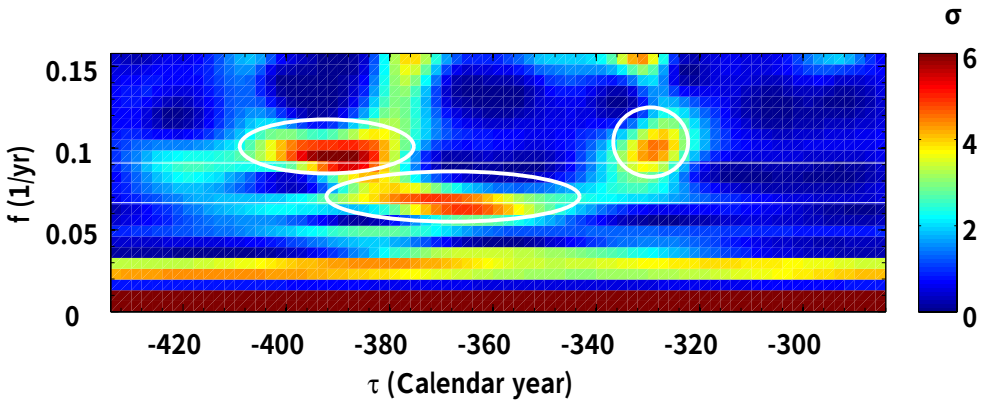

Figure 4.8: The x-axis and the y-axis are the same as those in Figure 4.3 (p 65), but the color scale represents $\sigma(\tau, f)$. The two white horizontal lines represent $f = 1/11$ and $f = 1/15$ (1/yr).

It must be noted that the $\sigma(\tau, f)$ (Equation 4.14, p 69) is different from a commonly-used σ of a normal distribution. For example, 95 % confidence level corresponds to 3 σ in an exponential distribution, meanwhile it corresponds to 2 σ in a normal distribution. Two cumulative distribution functions (exponential distribution and normal distribution) are compared in Figure 4.9 (p 72).

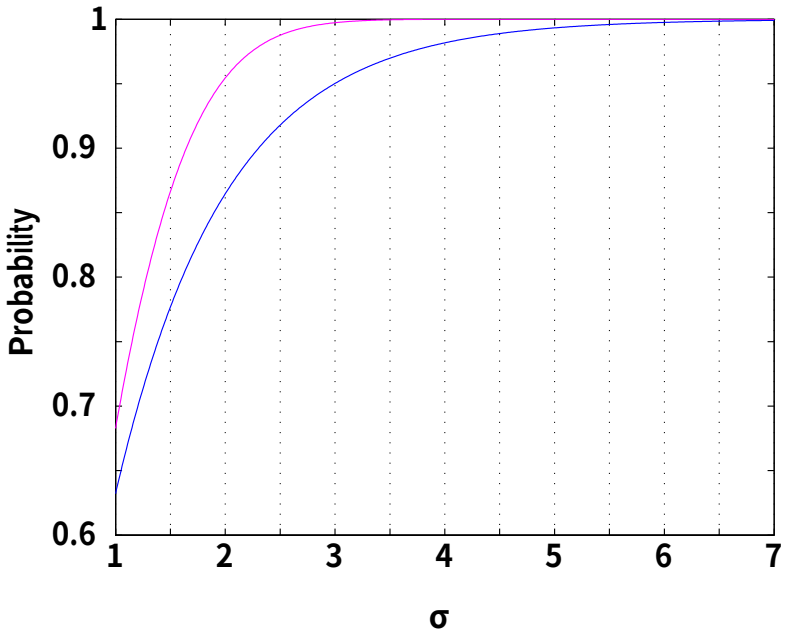

Figure 4.9: Cumulative distribution functions of the normal distribution (pink) and the exponential (blue) distribution. The y-axis represents the probability and the x-axis represents the variable which is normalized by the standard deviation.

4.7 Reconstruction of the Schwabe cycle

By using the bandpass filter, solar signal is extracted from the present Δ^{14}C record, $C_r(t)$. The bandwidth is selected as 1/18-1/9 (year^{-1}), which includes the frequency of the three significant regions of (τ, f) space (Figure 4.7, p 70 or Figure 4.8, p 71). Figure 4.10 (p 73) represents the extracted solar signal from the Δ^{14}C record. It seems that there are 12 cycles in the present Δ^{14}C record. The starting ages of 12 solar cycles (solar minimum in Figure 4.10, p 73) and their intervals are listed in Table 4.4 (p 74). Since the shapes of Δ^{14}C peaks (solar minimum)

of 6th and 7th cycles are not clear, the average of two adjacent solar maximum ages were applied to the 6th and 7th starting ages. The cycle lengths are around 11 years in the 1-4th and in the 8-12th cycles, while they are around 16 years in the 5-7th cycles, as shown in Table 4.4 (p 74).

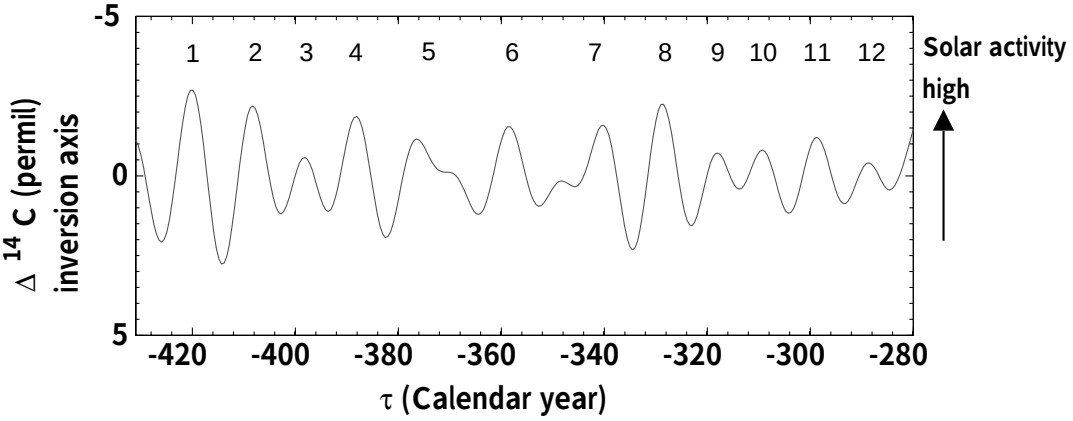

Figure 4.10: The extracted solar signal from the present Δ^{14}C record by using the bandpass filter with a 1/18-1/9 (year^{-1}) band. The x-axis represents the calendar year, and the y-axis represents the Δ^{14}C (‰). The scale of y-axis is inverted so that the upper direction represents the high solar activity. The numbers in the upper part of the figure represent the solar-cycle number which are defined as starting from around 430 BC.

Table 4.4: The cycle numbers, the ages of solar minima and maxima of 12 solar cycles, and their cycle lengths (interval of adjacent two solar minima) which are indicated by the bandpass filtered signal.

Cycle No.	Minimum	Maximum	Interval (years)
1	-426	-420	12
2	-414	-408	9
3	-403	-398	10
4	-393	-388	11
5	-382	-376	16
6	-366	-358	17
7	-349	-340	14
8	-335	-329	12
9	-323	-318	9
10	-314	-309	10
11	-304	-299	10
12	-294	-288	9
13	-285	-	-

To estimate the detection significance of the 12 solar cycles detected in the present Δ^{14}C record, $\sigma(\tau, f)$ is averaged between the ages of two adjacent solar minima with respect to each frequency, thus $\sigma(f)$ of 12 cycles are obtained. The $\sigma(f)$ in 12 cycles are shown in Figure 4.11 (p 76). In the 3-6th and 8th cycles, the mximum value of the $\sigma(f)$ exceed 3 σ as shown in Figure 4.11. Thus the 3-6th and 8th cycles seem to be detected with sufficient significance (more than 3σ or 95% confidence level). The $\sigma(f)$ of the 3rd, 4th, and 8th cycles exceed 3 σ in the cycle

lengths of around 11 years, and the 5th and 6th cycles are also significant in that of around 15 years. Similarly, the mximum value of the $\sigma(f)$ in the 1st, 2nd, 7th, and 9th cycles are 2-3 σ. The 1st, 2nd, and 9th are significant in the cycle lengths of around 11 years, and the 7th cycle is significant in that of around 15 years. The 10-12th cycles are not significant with less than 1 σ in all cycle lengths. The $1/f$ (years) which gives mximum $\sigma(f)$ is feasible cycle length in each cycle. The $1/f$ (years) which gives mximum $\sigma(f)$, and the maximum value of the $\sigma(f)$ of 12 cycles are listed in Table 4.5 (p 77).

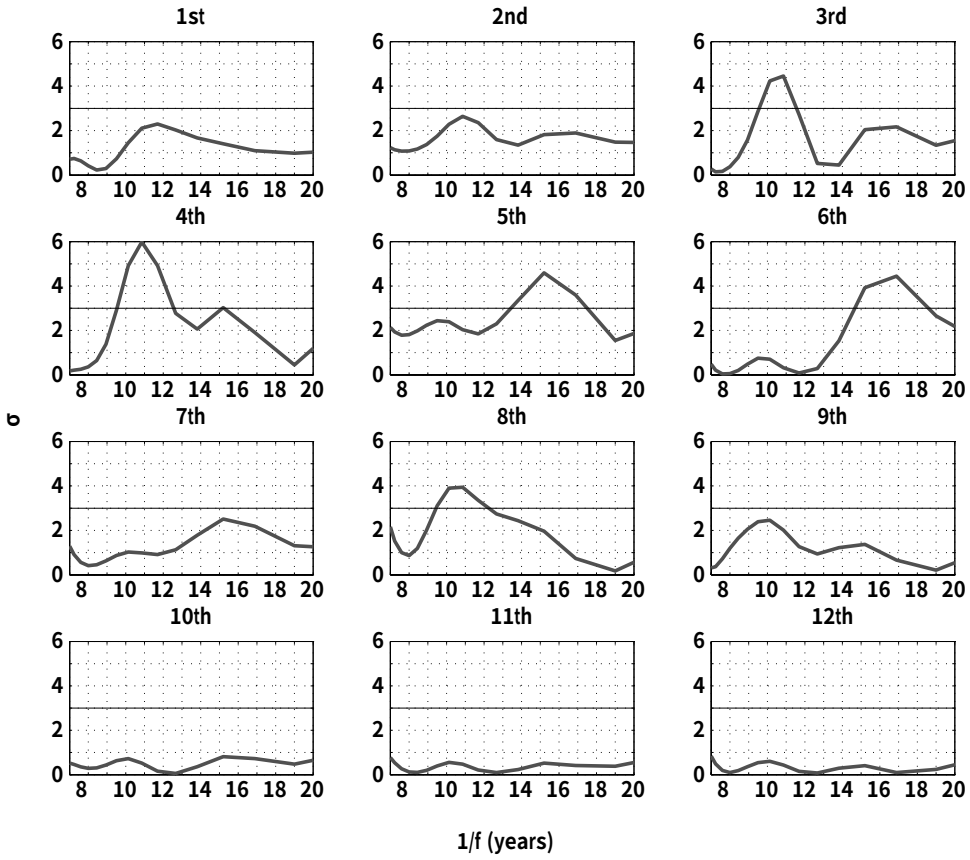

Figure 4.11: The significance, σ of the cycle lengths of the 12 solar cycles. The x-axis represents the cycle length, $1/f$ (year), and the y-axis represents the significance, $\sigma(f)$. The titles of figures represent the cycle number.

Table 4.5: The cycle length, $1/f$ (years) which gives mximum $\sigma(f)$, and the maximum value of the $\sigma(f)$ of the 12 cycles.

Cycle No.	$1/f$ (years)	$\sigma(f)$
1	12	2-3
2	11	2-3
3	11	≥ 3
4	11	≥ 3
5	15	≥ 3
6	17	≥ 3
7	15	2-3
8	10.5	≥ 3
9	10	2-3
10	10	≤ 1
11	10	≤ 1
12	10	≤ 1

The error of the ages of the 12 solar minima, maxima, and cycle lengths are estimated by the Monte Carlo simulation. Normally distributed random variables, whose expected value is the present Δ^{14}C record, $C_r(t)$ and standard deviation is the $E_r(t)$ (Table 4.3, p 61), were generated. This data set is considered as simulated Δ^{14}C record, and simulated solar cycle signal ($f = 1/18 - 1/9$ year^{-1}) is extracted from this data set by using the bandpass filter. The simulated solar cycle signal is spline-interpolated, and time series of differential and second order differential are computed. Then the ages, when the time series

of the differential reduced to zero and the second order differential is positive (local maxima of the simulated Δ^{14}C record), are considered as simulated solar minima. Similarly local minima of the simulated Δ^{14}C record are considered as simulated solar maxima. The simulated solar minima (maxima) corresponding to the each observed minima (maxima) of the cycle 1-12 are seeked between the ages of two adjacent observed maxima (minima). The simulated solar minima corresponding to the observed minima of the only 6th and 7th cycles are defined as intermediate value of the simulated solar maxima of the 5th and 6th cycles (for the 6th minimum), and 6th and 7th cycles (for the 7th minimum). If the multiple simulated solar minima (maxima) corresponding to one observed minima (maxima) were obtained, the highest (lowest) peak (bottom) is applied to the simulated solar minima (maxima). Simulated cycle lengths are defined as the interval of two adjacent simulated solar minima. An example of the simulated solar cycle signal out of 100,000 simulations is shown in Figure 4.12 (p 79).

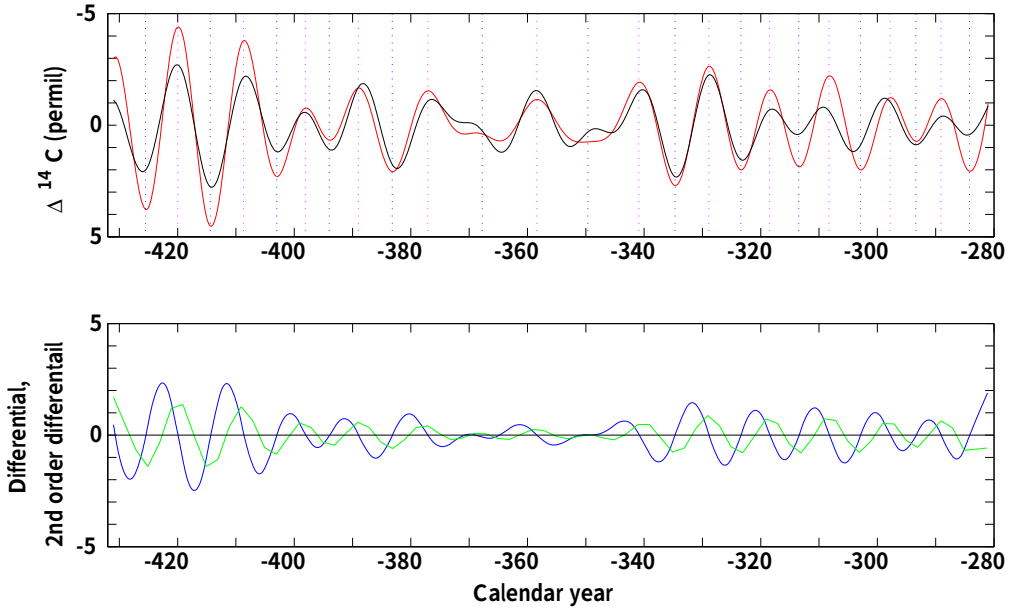

Figure 4.12: An example of the simulated solar cycle signal out of 100,000 simulations. In the upper panel, black curve represents the observed solar cycle signal, red curve represents an example of the simulated solar cycle signal, vertical magenta lines represents the simulated solar minima, and vertical magenta lines represents the simulated solar maxima. In the lower panel, blue curve represents the time series of differential of the simulated solar cycle signal (the red curve in the upper figure) and green curve represents the second order differential of the same with blue curve.

These calculations are repeated 100,000 times, and probability density distributions of the ages of the solar minima, maxima, and the cycle lengths of the 12 cycles were obtained. The 100,000 simulated solar cycle signals of each age are distributed around the original bandpass filtered signal (observed solar cycle signal) (Figure 4.10, p 73) by Gaussian distribution. Expected value and error range of the simulated solar cycle signals are shown in Figure 4.13 (p 80). However, it must be noted that each data point of the simulated solar cycle signals never varies independently from several data points around itself, because the simu-

lated solar cycle signal is sum of sine functions whose frequency band is $f = 1/18 - 1/9$ year^{-1}.

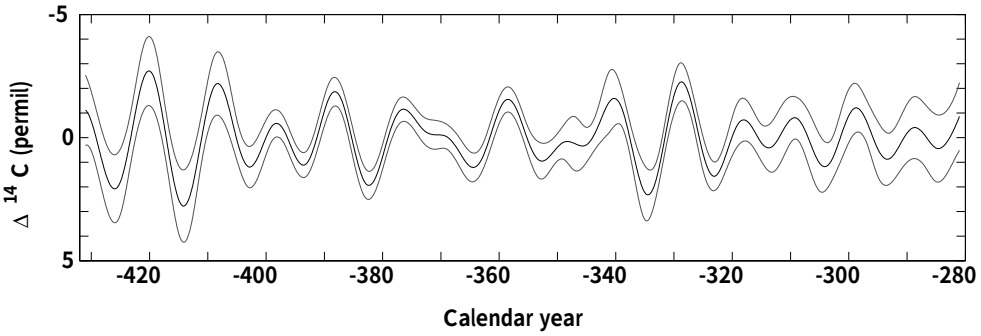

Figure 4.13: The expected value and the error range of the simulated solar cycle signals by using the bandpass filter.

Histogram of the number of the simulated solar minima and maxima corresponding to the each observed 12 solar cycles are shown in Figure 4.14 (p 81) and Figure 4.15 (p 82). Figure 4.14 and Figure 4.15 shows that the simulated solar minima (maxima) almost correspond to the observed 13 solar minima (12 maxima) one for one respectively. The solar maxima of 5th and 7th cycles often has double bottoms because of the small dips around 370 BC and 350 BC as shown in Figure 4.13 (p 80). Herewith the solar minima of 6th and 7th cycles also have double peaks.

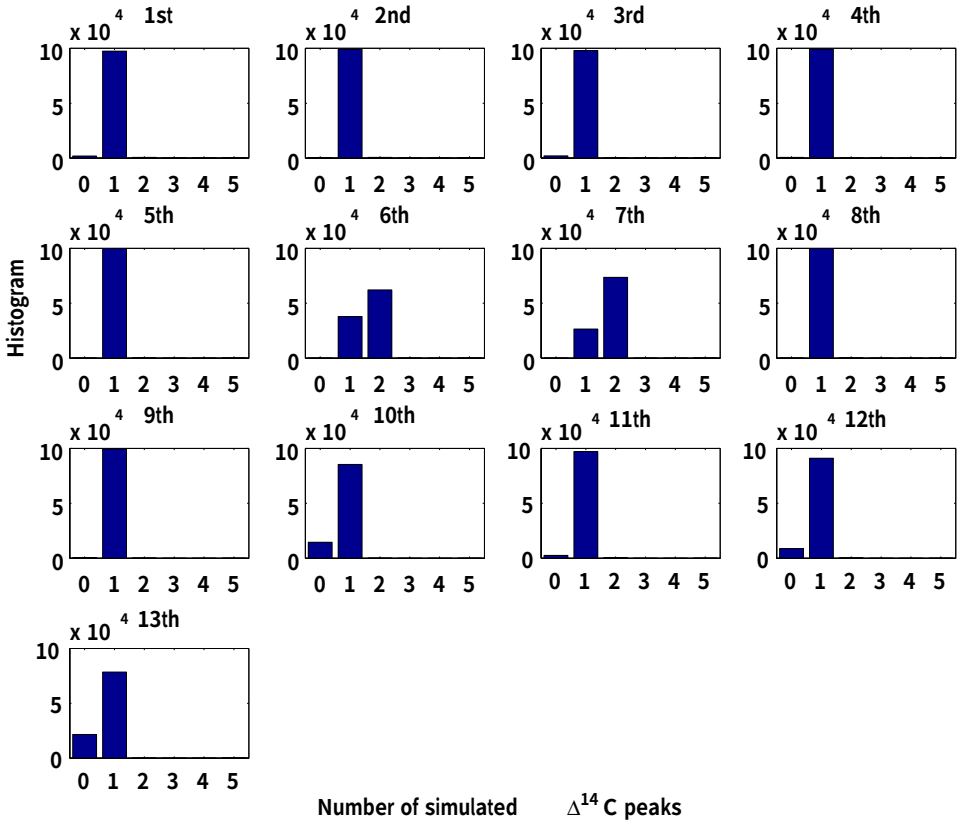

Figure 4.14: Histogram of the number of the simulated solar minima of the 13 cycles.

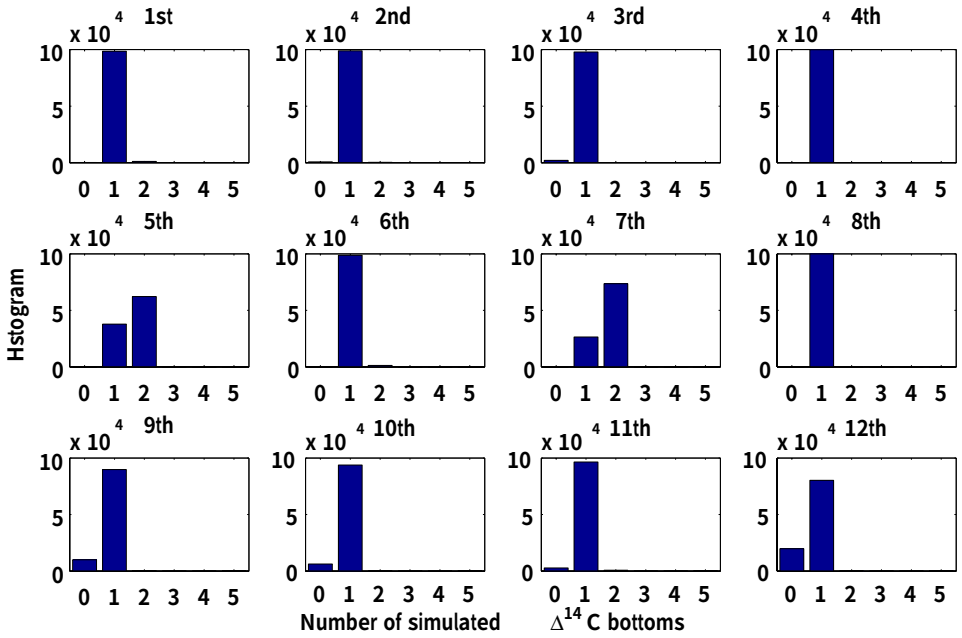

Figure 4.15: Histogram of the number of the simulated solar maxima of the 12 cycles.

Probability density distribution of the ages of the simulated solar minima, maxima, and the cycle lengths are fitted by Gaussian distribution function or sum of two Gaussian distribution functions. The probability density distributions of the ages of the simulated 13 solar minima and 12 solar maxima are shown in Figure 4.16 (p 83) and Figure 4.17 (p 84).

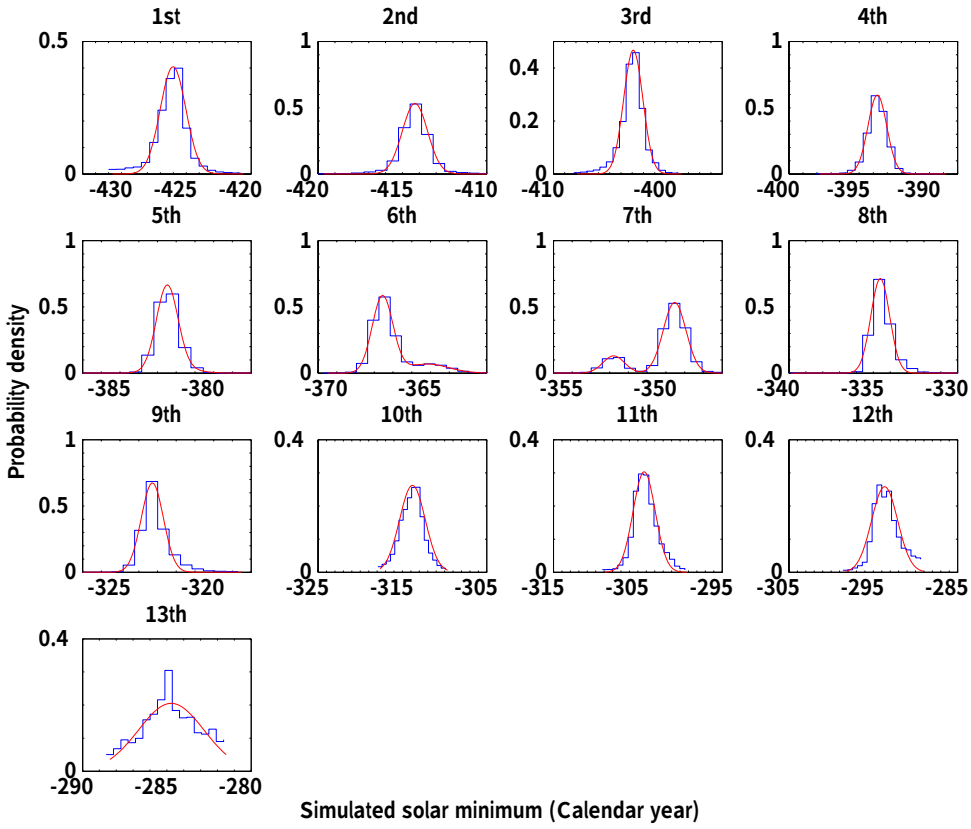

Figure 4.16: Probability density distributions of the ages of the simulated solar minima of the 13 cycles by using the bandpass filter.

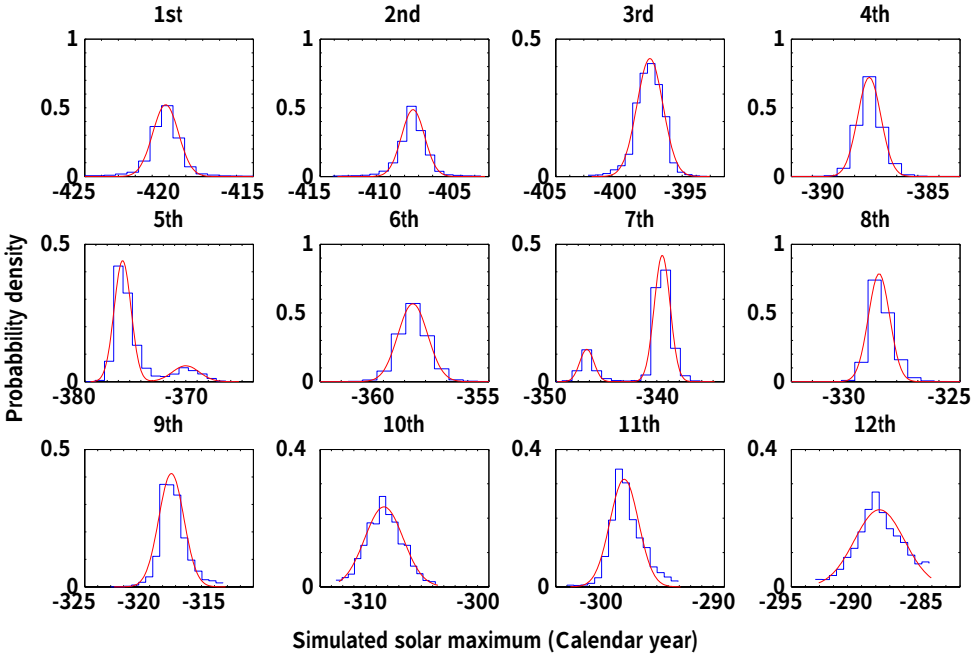

Figure 4.17: Probability density distributions of the ages of the simulated solar maxima of the 12 cycles by using the bandpass filter.

The distributions of solar maxima of 5th and 7th cycles have double peaks because of the small dips around 370 BC and 350 BC as shown in Figure 4.13 (p 80). Herewith the distributions of solar minima of 6th and 7th cycles also have double peaks. Amplitudes of these small dips are very low, so these short cycles are not significant in the $\sigma(\tau, f)$ as shown in Figure 4.8 (p 71). Therefore the small dips are considered to be negligible, and the simulated cycle lengths are determined. Probability density distributions of the simulated solar-cycle lengths of the 12 cycles are shown in Figure 4.18 (p 85). The expected values and errors (one standard deviation) of the ages of 13 solar minima, 12 solar maxima, and 12 cycle lengths are listed in Table 4.6 (p 86). It must be noted

that these ages of solar minima and maxima will simultaneously shift to several years older ages due to the phase lag between the variation of the carbon-14 production rate and the variation of the atmospheric carbon-14 concentration, which is caused by the carbon cycle.

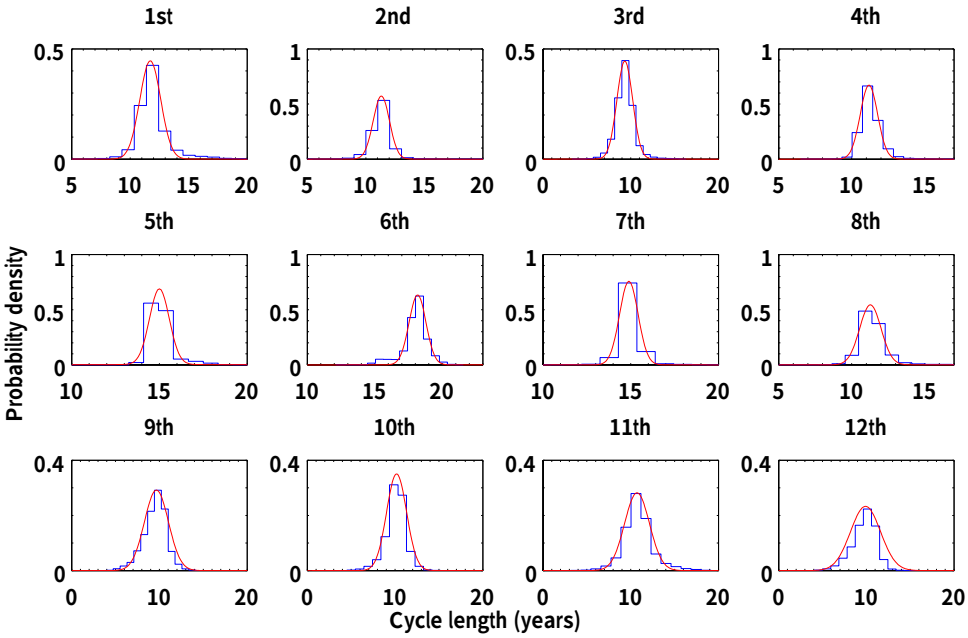

Figure 4.18: Probability density distributions of the simulated solar-cycle lengths of the 12 cycles by using the bandpass filter.

Table 4.6: The cycle numbers, the expected values and errors (one standard deviation) of the ages of the 13 solar minima and the 12 solar maxima, and their cycle lengths (interval of adjacent two solar minima) by using the bandpasss filter. It must be noted that these ages of the solar minima and maxima may simultaneously shift to several years older ages due to the phase lag by carbon cycle.

Cycle No.	Minimum	Maximum	Interval (years)
1	-426.0±1.0	-420.2±0.8	11.7±0.9
2	-414.2±0.8	-408.4±0.8	11.3±0.8
3	-402.9±0.8	-398.3±0.9	9.3±0.9
4	-393.7±0.7	-388.3±0.6	11.2±0.6
5	-382.6±0.5	-376.6±0.8	14.9±0.5
6	-367.6±0.5	-358.6±0.7	18.2±0.6
7	-349.5±0.6	-340.5±0.6	14.9±0.5
8	-334.6±0.6	-328.8±0.5	11.3±0.7
9	-323.2±0.6	-318.3±1.0	9.7±1.3
10	-313.8±1.5	-309.3±1.7	10.2±1.1
11	-304.3±1.3	-298.9±1.3	10.7±1.4
12	-293.7±1.6	-288.9±2.1	9.9±1.7
13	-284.4±2.3	-	-

The errors of the cycle lengths which are determined by using S-transform are also estimated by a Monte Carlo simulation similar to the case of using bandpasss filter. The simulated Δ^{14}C record is generated by the same way and converted into the power spectrum, $P(\tau, f)$ by using S-transform. The simulated power spectrum, $P(\tau, f)$ is divided

by $\mu(\tau, f)$, and simulated $\sigma(\tau, f)$ is obtained. The simulated $\sigma(\tau, f)$ is averaged between the age of a solar minimum and next solar minimum with respect to each cycle, and $\sigma(f)$ is obtained. Simulated cycle length is determined as the $1/f$ (years) which gives maximum $\sigma(f)$ with respect to each cycle. These calculations are repeated 100,000 times, and probability density distributions of 12-cycle lengths are obtained, which are fitted by Gaussian distribution function. The simulated probability density distributions of 12-cycle lengths and the fitting curves are shown in Figure 4.19 (p 87). The expected values and errors (one standard deviation) of cycle lengths of 12 solar cycles are listed in Table 4.7 (p 88).

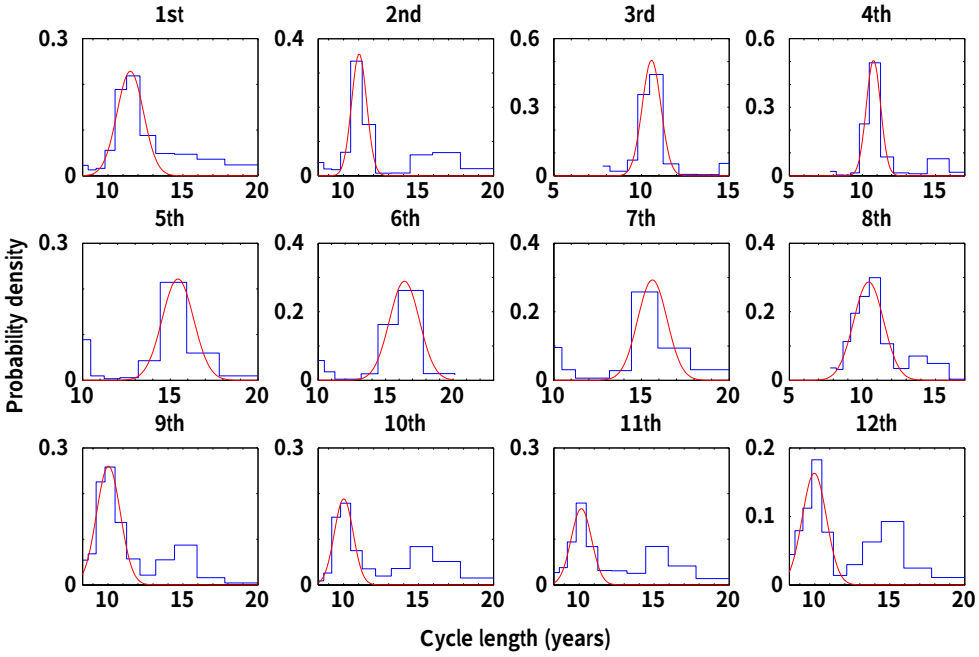

Figure 4.19: Probability density distributions of the simulated solar-cycle lengths of the 12 cycles by using S-transform.

Table 4.7: The expected values and the errors (one standard deviation) of the cycle lengths of the 12 solar cycles by using S-transform.

Cycle No.	$1/f$ (years)
1	11.5±1.2
2	11.0±0.7
3	10.6±0.8
4	10.8±0.7
5	15.4±1.3
6	16.4±1.6
7	15.6±1.2
8	10.4±1.4
9	10.0±1.1
10	10.0±0.9
11	10.1±1.0
12	10.0±1.1

The two expected values and errors (one standard deviation) of cycle lengths with respect to 12 solar cycles, which are individually estimated by using bandpass filter and S-transform, are shown and compared with the modern solar-cycle lengths in Figure 4.20 (p 89). The two results of the individual estimations of the cycle lengths agree with each other. The cycle lengths of the 5-7th cycles are likely to be longer than the average of the modern 22 cycles (Table 2.1, p 10), whereas those of 1-4th and 8-12th cycles are comparable to the modern average.

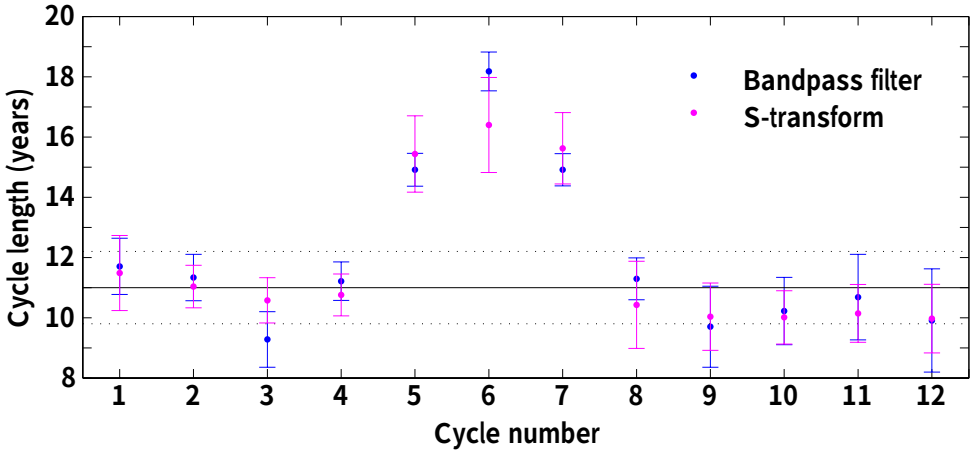

Figure 4.20: The expected values and the errors (one standard deviation) of the cycle lengths of the 12 solar cycles, which are individually estimated by using the bandpass filter (blue dots and error bars) and S-transform (magenta dots and error bars). Black horizontal lines represent the average of modern 22 solar-cycle lengths (solid line) and the standard deviation (dashed line) (Table 2.1, p 10).

Chapter 5

Discussion

5.1 Schwabe cycle length during the BC4 Minimum

Present Δ^{14}C record, $C_r(t)$ (Figure 4.2), the result of the periodicity analysis, $A(\tau, f)$ (Figure 4.3), confidence level from the Monte Carlo simulation, $\sigma(\tau, f)$ (Figure 4.8), and filtered Δ^{14}C record (Figure 4.10) are shown together in Figure 5.1 (p 91).

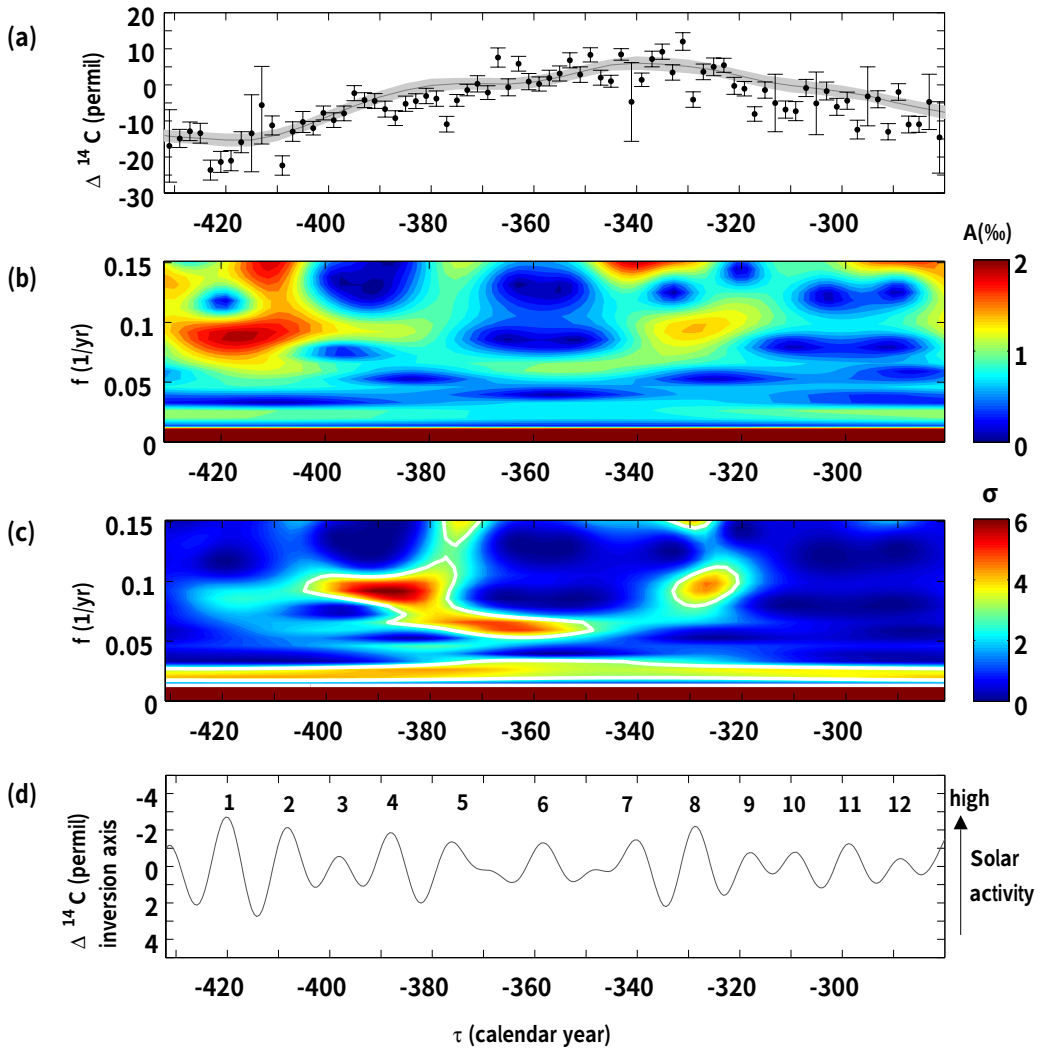

Figure 5.1: (a) Present Δ^{14}C record, C_r and IntCal. (b) Contour plot of the amplitude spectrum, $A(\tau, f)$ from the C_r by S-transform. (c) Contour plot of the significance of the $A(\tau, f)$, $\sigma(\tau, f)$. (d) Filtered C_r for a frequency band of 1/18-1/9 (year^{-1}).

Periodicity analysis reveals three significant signal regions of 11-year and 15-year periods, as shown in Figure 5.1 (c) (p 91). These signals seem to be related to the Schwabe cycle, because the cycle lengths are

close to those of the modern SSN cycles (ca. 11.0±1.2 years as stated in section 2.1). In addition, the double-length periodicity of approximately 22 years and 30 years, which corresponds to the Hale cycle, are observed in $A(\tau, f)$ (Figure 5.1 (b), p 91) at the same time with the 11-year and the 15-year periodicities, although it is not so significant in $\sigma(\tau, f)$ (Figure 5.1 (c), p 91). These double-length periodicity correspond to the Hale cycle which may appear together with the Schwabe cycle as stated in section 2.1. The amplitudes of the 11-year and the 15-year periodicities are ±1-2 ‰ (Figure 5.1 (b), p 91). These amplitudes are consistent with the value which is estimated from the amplitude of the ^{14}C production variation (about ±15 %) attributed to the Schwabe cycle, and amplitude attenuation by the carbon cycle (the attenuation rate is 1/100), as stated in section 2.4. Actually, Stuiver et al. (1998) and Miyahara et al. (2004; 2008; 2010) obtained Δ^{14}C record of 1-2 year time resolution and the Schwabe cycle was detected from their data, those amplitudes are ±1-3 ‰ by Miyahara et al. (2004; 2008; 2010). These amplitudes seem to be comparable level with present result in the 4^{th} century BC. Therefore, it is consistent that the significant signals in $\sigma(\tau, f)$ are considered to be related to the Schwabe cycle. The evidence for the ancient Schwabe cycle has been found in the 10^{th} (Miyahara, Yokoyama, and Masuda, 2008), 14^{th} (Miyahara et al., 2010), and 17^{th} centuries (Beer, 1998; Miyahara et al., 2004; Berggren et al., 2009). Therefore, the present result is the oldest evidence of the Schwabe cycle at the present time.

By the Monte Carlo simulations, two results of the 12 cycle-lengths

and errors were estimated as shown in Figure 4.20 (p 89). Here, the result which has a larger error between the two results with respect to 12 cycles are listed together with the age of the solar minimum and the detection significance (the maximum value of the $\sigma(f)$) in Table 5.1 (p 94). Schwabe cycle lengths of the 5-7th cycles are likely to be several years longer than the modern average of 11.0±1.2 years as shown in Figure 4.20 (p 89). On the other hand, the cycle lengths of the 1-4th and 8-12th cycles are comparable to the modern average. However, the 10-12th cycles can not be separated from the noise components, whereas the 3-6th and 8th cycles are sufficiently significant, and the 1st, 2nd, 7th, and 9th cycles are less significant as shown in Table 5.1 (p 94). Therefore, the Schwabe cycle lengths in the 5th and 6th cycles are significantly several years longer than the modern average, and possibly, that of the 7th cycle is also longer than the modern average. Prolonged sunspot absence in the 4^{th} century BC is estimated to be about 400-320 BC from the record of the carbon-14 production variation by Stuiver and Braziunas (1988). The 5-7th cycles are included in the period of the estimated prolonged sunspot absence as seem from Table 5.1 (p 94). The increase of the cycle length in the period of prolonged sunspot absence confirms the inverse correlation between the amplitude and length of the Schwabe cycle (Solanki et al., 2002; Hathaway et al., 2002; Watari, 2008).

Table 5.1: The cycle number, the age of the solar minimum, the cycle length (years), and the detection significance (the maximum $\sigma(f)$) of each cycle. The ages of solar minima may simultaneously shift to several years older ages due to the phase lag by carbon cycle.

Cycle No.	Minimum	Length (years)	$\sigma(f)$
1	-426.0±1.0	11.5±1.2	2-3
2	-414.2±0.8	11.3±0.8	2-3
3	-402.9±0.8	9.3±0.9	≥ 3
4	-393.7±0.7	10.8±0.7	≥ 3
5	-382.6±0.5	15.4±1.3	≥ 3
6	-367.6±0.5	16.4±1.6	≥ 3
7	-349.5±0.6	15.6±1.2	2-3
8	-334.6±0.6	10.4±1.4	≥ 3
9	-323.2±0.6	9.7±1.3	2-3
10	-313.8±1.5	10.2±1.1	≤ 1
11	-304.3±1.3	10.7±1.4	≤ 1
12	-293.7±1.6	9.9±1.7	≤ 1

5.2 Characteristics of the Schwabe cycle in the four grand solar minima

In terms of the phenomenological prediction of grand solar minima, it is important to study the transition of cycle lengths just before the onset of a period of prolonged sunspot absence. In this section, the temporal change of the length of the Schwabe cycle in the BC4 Minimum is com-

pared to that in the Spörer Mininmum, the Maunder Minimum, and the Dalton Minimum to discuss the general feature of the cycle length change in grand solar minima. The temporal change of the Schwabe-cycle length in the above three grand solar minima has been discussed by Miyahara et al. (2010) as stated in section 2.5. During the period of the Maunder Minimum, the length of the Schwabe cycle was approximately 10 years around 1605 AD (the onset of the carbon-14 increase), and is considered to subsequently increase to 12-13 years around the onset of the prolonged sunspot absence, and then be maintained at approximately 14 years after 1660 AD (Miyahara et al., 2010). In the case of the Spörer Mininmum, which is one of S-type grand solar minima, the cycle lengths increased to about 13 years, but only for the 2 cycles before the onset of estimated prolonged sunspot absence. In the case of the Dalton Minimum, which is one of W-type grand solar minima, the preceding solar cycle is about 13 years, although only for a single cycle starting at around AD 1784.

In the case of the BC4 Minimum, which is one of M-type grand solar minima, prolonged sunspot absence is estimated to be about 400-320 BC from the record of the carbon-14 production variation by Stuiver and Braziunas (1988). Taking the several years phase lag by the carbon cycle into consideration, the onset of the prolonged sunspot absence in the BC4 Minimum might correspond to the 3rd or 4th cycle in the present Δ^{14}C record. The cycle lengths of the 3rd and 4th cycles are 9.3$\pm$0.9 years and 10.8$\pm$0.7 years, and the detection significances of both cycles exceed 3σ (Table 5.1, p 94). Therefore, the cycle lengths less likely to have

increased relative to the modern average at the onset of the prolonged sunspot absence in the BC4 Minimum, although it increased by several years during the estimated prolonged sunspot absence. The properties of the Schwabe cycle in the four grand solar minima discussed in this section are summarized in Table 5.2 (p 96) together with that of the normal activity in the modern period.

Table 5.2: Comparison of the Schwabe cycle properties. The event name of solar activity, the age of the event, the type of grand solar minima, the characteristic Schwabe cycle length, and timing of the characteristic Schwabe cycle length in grand solar minima related to the prolonged sunspot absence are shown respectively.

Event name	Age (century)	Type	Cycle length (years)	Timing
BC4 M.	4^{th} BC	M	15.4±1.3, 16.4±1.6	within
Spörer M.	13^{th}	S	13	preceding
Maunder M.	17^{th}	M	14	within
Dalton M.	19^{th}	W	13	preceding
Normal activity	18-20^{th}	-	11.0±1.2	-

Schwabe cycle lengths increased in all of the four minima from ancient time to modern time compared with that in modern normal activity, which is listed in the last line of Table 5.2, nevertheless there are differences in the cycle length (the fourth column in the same table) and

timing (the fifth column in the same table). The relation between the grand solar minima and increase of the Schwabe cycle length is confirmed more strongly by the present study. The Schwabe cycle lengths in two M-type minima dynamically increased with prolonged sunspot absence and the lengths were longer than that in the other two minima, although the cycle lengths increased prior to the onset of the prolonged sunspot absence in the Spörer and the Dalton Minima. Thus the grand solar minima classified according to their duration may have different patterns of variation with respect to the Schwabe cycle length. To determine the Schwabe cycle lengths around the onset of the (estimated) prolonged sunspot absence more precisely and to determine the type of minima (e.g., grand solar minimum in the 8^{th} century BC is another S-type minimum than the Spörer Minimum) may be the subjects for a further study.

5.3 The trigger of prolonged sunspot absence indicated from solar dynamo model

The association between the increase of the Schwabe-cycle length by a few years and the grand solar minima has been confirmed by the present study. There are a number of works that attempt to theoretically reproduce periods of prolonged sunspot absence, such as the Maunder Minimum, by allowing variation of the dynamo parameters (Charbonneau

and Dikpati, 2000; Usoskin et al., 2009; Choudhuri and Karak, 2009; Karak, 2010). In particular, Karak (2010) reproduced the prolonged sunspot absence in the Maunder Minimum using the flux transport dynamo model with the assumption that the meridional-circulation velocity was decreased for several years at the onset of the sunspot absence, and then recovers within several decades by around 1680 AD as shown in Figure 5.2 (p 100). In the flux transport dynamo model, meridional-circulation velocity is inversely correlated to the length of the Schwabe cycle (Dikpati and Charbonneau, 1999; Hotta and Yokoyama, 2010). From the observations of sunspots, a positive correlation between the Schwabe cycle amplitude and the meridional circulation velocity (Hathaway et al., 2003) and a negative correlation between the Schwabe cycle length and the amplitude (Solanki et al., 2002; Hathaway et al., 2002; Watari, 2008) have been suggested. Therefore, the assumption of a decrease in the meridional-circulation velocity suggests an increase of the cycle length in the early stage of the prolonged sunspot absence in the grand solar minima. Miyahara et al. (2010) pointed out that the cycle length started to increase at 1 or 2 cycles before the onset of the estimated prolonged sunspot absence in the Spörer Minimum, Maunder Minimum, and the sunspot decrease in the Dalton Minimum. In the case of the Maunder Minimum and the BC4 Minimum, the longest cycle(s) appears at the first half of the prolonged sunspot absence or the estimated prolonged sunspot absence. The assumption by Karak (2010) is not the only solution; however, this timing correspondence is notewor-

thy for investigation of the upstreamer trigger of the grand solar minima. Precise studies of the processes of cycle-length change around the onset of the (estimated) prolonged sunspot absence should be conducted. The temporal profiles of the Schwabe cycle length in the grand solar minima may give the limitation and improve these dynamo models. Many researches have predicted the next (cycle 24) solar maximum date and the amplitude of the sunspot number by using the various methods (Pesnell, 2008). Some researches have used the flux transport dynamo models as the tool of the prediction (Dikpati and Gilman, 2008; Choudhuri, 2008). At some future date, dynamo models possibly predict the more long-term solar activity such as the Maunder Minimum. The present study might slightly contribute for such a future.

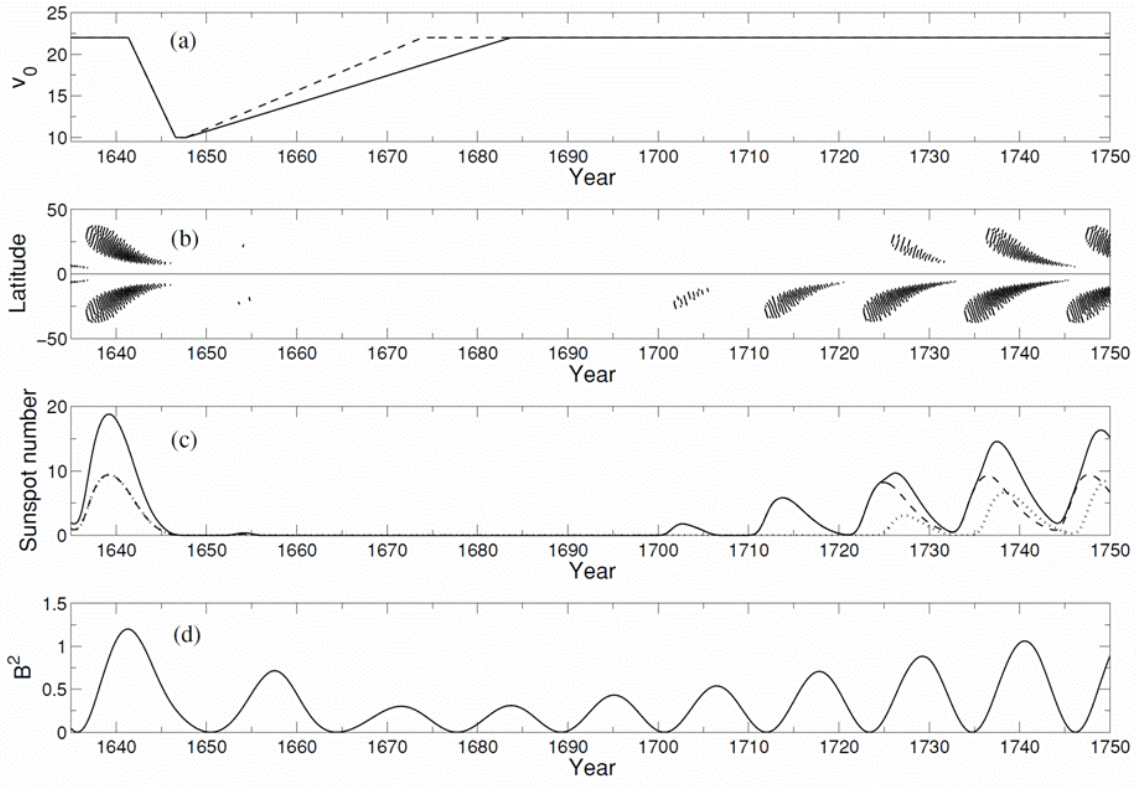

Figure 5.2: Reproduced prolonged sunspot absence by Karak (2010). (a) The assumption of the variation of the meridional circulation velocity (in ms^{-1}) in the dynamo model. (b) The theoretical butterfly diagram. (c) The theoretical sunspot number. The dashed and dotted lines show the sunspot numbers in southern and northern hemispheres, whereas the solid line is the total sunspot number. (d) Variation of energy density of the toroidal field at at the bottom of the convection zone.

5.4 Climate around the 4^{th} century BC

The present study confirms that the large increase of Δ^{14}C in the 4^{th} century BC indicates the presence of prolonged sunspot absence similar to the Maunder Minimum. IntCal data suggests another Spörer-type minimum in the 8^{th} century BC (the BC8 Minimum). The multi-proxy reconstructed climate traced back to 3000 years ago indicates cooling and/or

wetter shifting around the 8^{th} century BC in Europe and others, and this climatic event is associated with the BC8 Minimum (Geel et al., 1996; Plunkett and Swindles, 2008). This climatic event has been recorded globally (Geel et al., 1996; and references therein). Some researches indicate another climatic event associated with the BC4 Minimum other than the BC8 Minimum (Barber and Langdon, 2007; Swindles et al., 2007; Berner et al., 2008). In addition, there are some researches that indicate the climatic event around the 8^{th} century BC may have lasted to include not only the period of the BC8 Minimum but also the period of the BC4 Minimum (Desprat et al., 2003; Garcia et al., 2007). The sequence of the grand solar minima in the 8^{th} century BC and the 4^{th} century BC may have influenced the Earth's cooling, similar to the LIA in the past millennium, which is considered to have been caused by the sequence of the Wolf Minimum, the Spörer Minimum, and the Maunder Minimum. This possible association might increase an importance of long-term solar variability in considering the origin of the Earth's climate changes on a centurial to millennial time scale.

Chapter 6

Conclusion

In the present study, the variation of the Schwabe cycle length during the grand solar minimum of the 4^{th} century BC was determined by measurements of the atmospheric carbon-14, which are stored in annual tree rings, as an index of the solar variability.

The tree sample was a camphor tree excavated from the bottom of Fukushima River, Miyazaki in southern Japan. The carbon-14 concentrations in single tree rings were measured by using two accelerator mass spectrometers at Nagoya University and the University of Tokyo. Multiple targets were prepared for each tree ring of the same year to achieve high statistical precision and to conduct an assessment of the systematic reproducibility. Thus the biennial time series of the Delta C-14 during 431-281 BC was obtained.

The signal of the Schwabe cycle was detected in the present Delta C-14 record by the wavelet analysis, and the statistical confidence level

was assessed by using the Monte Carlo simulation. As a result, twelve cycles of the Schwabe cycle were detected in the present Delta C-14 record. The signals of 3-6th and 8th cycles were sufficiently significant (confidence level of higher than 95%). The present result is the oldest evidence for the Schwabe cycle of the solar activity at the present time.

The Schwabe cycle lengths and their errors were estimated by the Monte Carlo simulations. The cycle lengths of the 5th and 6th cycles are significantly several years longer than the modern average (normal activity), and that of the 7th cycle is possibly longer than the modern average also, whereas those of the 3rd, 4th, and 8th cycles were comparable with the modern average. Present study confirms the association between the long-term declination of the solar activity and the increase of the Schwabe cycle length more strongly.

The Schwabe cycle lengths during the BC4 Minimum and the Maunder Minimum, which are both M-type minima, dynamically increased within the period of the (estimated) prolonged sunspot absence. On the other hand, in the case of the Spörer Minimum (S-type) and the Dalton Minimum (W-type), the Schwabe cycle lengths increased 1-2 cycles prior to the onset of the estimated prolonged sunspot absence (or sunspot decrease). The grand solar minima, which are classified according to their duration time, may have the different patterns of the variation with respect to the Schwabe cycle length.

Karak (2010) reproduced the prolonged sunspot absence using the flux transport dynamo model with the assumption that the meridional-

circulation velocity was decreased for several years at the onset of the sunspot absence and then recovers gradually in several decades. A decrease of the meridional-circulation velocity at the onset of the prolonged sunspot absence suggests an increase of the Schwabe cycle length in the early stage of the prolonged sunspot absence. The observed cycle-length increase during the four grand solar minima (the BC4 Minimum, the Spörer Minimum, the Maunder Minimum, and the Dalton Minimum) may confirm the theoretical model of a prolonged sunspot absence by Karak (2010).

The reconstructed climate of the last 3,000 years indicates cooling and/or wetter conditions around the 8^{th} century BC globally and is associated with the grand solar minimum of the 8^{th} century BC. Some research indicates this climatic event may have lasted to include the period of the BC4 Minimum, although the evidences are found out not globally but locally. The sequence of the grand solar minima in the 8^{th} century BC and the 4^{th} century BC may have influenced the Earth's cooling period, similar to the Little Ice Age in the past millennium, which is considered to have been caused by the sequence of the Wolf Minimum, the Spörer Minimum, and the Maunder Minimum.

Acknowledgments

I would like to gratefully acknowledge Associate Prof. Kimiaki Masuda with deepest appreciation. He is my supervisor, and gave me this work and many helpful advices for completing this doctoral thesis. Likewise, I would like to express appreciation for Prof. Yoshitaka Itow (CR lab.), Prof. Toshio Nakamura (CCR), and Prof. Kanya Kusano (STEL), who gave me many useful suggestions, and thereby this thesis has been greatly improved.

I have learned a lot about the procedures of sample pretreatment, target preparation, and AMS operation from the staffs of CCR; Assistant Prof. Hirotaka Oda, Ms. Akiko Ikeda, and other people, and the staffs of MALT; Associate Prof. Hiroyuki Matsuzaki, Dr. Yosuke Miyairi, Ms. Yoko Sunohara, and other people. I really appreciate their many technical supports for the experiments.

I would like to thank the staffs of CR lab.; Emeritus Prof. Yasushi Muraki, Associate Prof. Yutaka Matsubara, Assistant Prof. Takashi Sako, Associate Prof. Fumio Abe, and Associate Prof. Takahiro Sumi (Osaka University), for many valuable discussions. I would like to thank

the members of our carbon-14 research team; Dr. Hiroko Miyahara (ICRR), Dr. Hiroaki Menjo (KMI), Mr. Kosuke Kuwana (graduate), Mr. Kyohei Kitazawa (graduate), Ms. Fusa Miyake. I have learned a lot from them, and had many discussions with them in the various phases of this work from planning the experiments to concluding finally. I would like to thank the members of CR lab.; Mr. Koki Kamiya (graduate), Dr. Gaku Mitsuka, Mr. Tsuyoshi Mase, Mr. Kei Furusawa, and other too many people to be mentioned here, for providing the comfortable academic life to me, and also thank Ms. Tomoyo Kainai for enormous office works.

Finally, I would like to give a special thanks to my parents who have supported my academic life for such a long time.

I could complete my work with the helps of the many people who are mentioned and can not be mentioned here. I would like to thank each and every one of them again.

This work was partially supported by the Grant-in-Aid for Nagoya University Global COE Program, "Quest for Fundamental Principles in the Universe: from Particles to the Solar System and the Cosmos", from the Ministry of Education, Culture, Sports, Science and Technology of Japan.

References

Babcock, H.D.: 1959, Astrophys. J. 130, 364, The Sun's Polar Magnetic Field.

Babcock, H.W.: 1961, Astrophys. J. 133, 572-587, The topology of the Sun's magnetic field and the 22-year cycle.

Barber, K.E. and Langdon, P.G.: 2007, Quat. Sci. Rev. 26, 3318-3327, What drives the peat-based palaeoclimate record? A critical test using multi-proxy climate records from northern Britain.

Beer, J., Tobias, S., and Weiss, N.: 1998, Solar Phys. 181, 237-249, An active sun throughout the Maunder Minimum.

Berggren, A.M., Beer, J., Possnert, G., Aldahan, A., Kubik, P., Christl, M., Johnsen, S. J., Abreu, J., and Vinther, B. M.: 2009, Geophys. Res. Lett. 36(11), L11801, A 600-year annual ^{10}Be record from the NGRIP ice core, Greenland.

Berner, K.S., Koc, N., Divine, D., Godtliebsen, F., and Moros, M.: 2008, Paleoceanography 23, 2, A decadal-scale holocene sea surface temperature record from the subpolar north atlantic constructed using diatoms and statistics and its relation to other climate parameters.

Bronk Ramsey, C., van der Plicht, J., and Weninger, B.: 2001, Radiocarbon 43, 381-389, 'Wiggle matching' radiocarbon dates.

Bronk Ramsey, C.: 2008, Quat. Sci. Rev. 27, 42-60, Deposition models for chronological records.

Charbonneau, P., and Dikpati, M.: 2000, Astrophys. J. 543, 1027-1043, Stochastic fluctuations in a Babcock-Leighton model of the solar cycle.

Choudhuri, A.R.: 2008, J. Astrophys. Astr. 29, 41-47, Prospects for predicting cycle 24.

Choudhuri, A.R. and Karak, B.B.: 2009, Res. Astron. Astrophys. 9, 953-958, A possible explanation of the Maunder Minimum from a flux transport dynamo model.

Desprat, S., Goni, M.F.S., and Loutre, M.F.: 2003, Earth Planet. Sci. Lett. 213, 63-78, Revealing climatic variability of the last three millennia in northwestern Iberia using pollen inxflux data.

Dikpati, M. and Charbonneau, P.: 1999, Astrophys. J. 518, 508-520, A Babcock-Leighton flux transport dynamo with solar-like Differential Rotation.

Dikpati, M.: 2008, Annales Geophysicae 26, 259-267, Predicting cycle 24 using various dynamo-based tools.

Dikpati, M., and Gilman, P.A.: 2008, J. Astrophys. Astr. 29, 29-39, Global solar dynamo models: Simulations and predictions.

Eddy, J.A.: 1976, Science 192, 1189-1202, The Maunder Minimum.

Geel, B.V., Buurman, J., and Waterbolk, H.T.: 1996, J. Quat. Sci. 11, 451-460, Archaeological and palaeoecological indications of an abrupt climate change in The Netherlands, and evidence for climatological teleconnections around 2650 BP.

Gil Garcia, M.J., Ruiz Zapata M.B., Santisteban, J.I., Mediavilla, R., Lopez-Pamo, E., and Dabrio, C.J.: 2007, Veget. Hist. Archaeobot. 16, 241-250, Late holocene environments in Las Tablas de Daimiel (south central in Iberian peninsula).

Godwin, H.: 1962, Nature 195, 984, Half-life of Radiocarbon.

Goslar, T.: 2003, PAGES News (Past Global Changes) 11(2-3), 12.

Hale, G.E., Ellerman, F., Nicholson, S.B., and Joy, A.H.: 1919, Astrophys. J. 49, 153-178, The magnetic polarity of sun-spots.

Hale, G.E. and Nicholson, S.B.: 1925, Astrophys. J. 62, 270, The law of sun-spot polarity.

Hathaway, D.H., Nandy, D., Wilson, R.M., and Reichmann, E.J.: 2003, Astrophys. J. 589, 665-670, Evidence that a deep meridional flow sets the sunspot cycle period.

Hathaway, D.H., Wilson, R.M., and Reichmann, E.J.: 2002, Solar Phys. 211, 357-370, Group sunspot numbers: sunspot cycle characteristics.

Hotta, H. and Yokoyama, T.: 2010, Astrophys. J. 709, 1009-1017, Importance of surface turbulent diffusivity in the solar flux-transport dynamo.

Hoyt, D.V. and Schatten, K.H.: 1998, Solar Phys. 179, 189-219, Group sunspot

numbers: A new solar activity reconstruction.

ICRU: 2010, Journal of the ICRU 10(2), 17-21, Cosmic-radiation fields at aircraft flight altitudes.

Jansen, E., and 48 lead and contributing authors: 2007, IPCC 2007: The physical science basis. Contribution of working group I to the fourth assessment report of the intergovernmental panel on climate change, Cambridge University Press, Cambridge, 433-497.

Joseph, R., and Wickramasinghe, N.C.: 2010, J. Cosmology 7, 1750-1770, Comets and contagion: Evolution and diseases from space.

Karak, B.B.: 2010, Astrophys. J. 724, 1021-1029, Importance of meridional circulation in flux transport dynamo: The possibility of a Maunder-like grand minimum.

Kota, J. and Jokipii, J.R.: 1983, Astrophys. J. 265, 573-581, Effects of drift on the transport of cosmic rays.

Leighton, R.B.: 1964, Astrophys. J. 140, 1547-1562, Transport of magnetic fields on the Sun.

Masarik, J. and Beer, J.: 1999, J. Geophys. Res. 104, 12099-12112, Simulation of particle fluxes and cosmogenic nuclide production in the Earth's atmosphere.

Matsuzaki, H., et al.: 2007, Nucl. Instrum. Methods Phys. Res. B 259, 36-40, Multi-nuclide AMS performances at MALT.

Maunder, E.W.: 1890, Mon. Not. R. Astron. Soc. 50, 251, Professor Spoerer's

researches on Sun-spots.

Miyahara, H., Masuda, K., Muraki, Y., Furuzawa, H., Menjo, H., and Nakamura, T.: 2004, Solar Phys. 224, 317-322, Cyclicity of solar activity during the Maunder Minimum deduced from radiocarbon content.

Miyahara, H., Nagaya, K., Masuda, K., Muraki, Y., Kitagawa, H., and Nakamura, T.: 2008, Quat. Geochronol. 3, 208-212, Transition of solar cycle length in association with the occurrence of grand solar minima indicated by radiocarbon content in tree-rings.

Miyahara, H., Yokoyama, Y., and Masuda, K.: 2008, Earth Planet. Sci. Lett. 272, 290-295, Possible link between multi-decadal climate cycles and periodic reversals of solar magnetic field polarity.

Miyahara, H., Kitazawa, K., Nagaya, K., Yokoyama, Y., Matsuzaki, H., Masuda, K., Nakamura, T., and Muraki, Y.: 2010, J. Cosmology 8, 1970-1982, Is the Sun heading for another Maunder Minimum? - Precursors of the grand solar minima.

Nagaoka, S., et al.: 1998, in T. Nakamura (ed), Summaries of Researches Using AMS at Nagoya University IX, the Nagoya University Center for Chronological Research, Nagoya Japan, p. 260-271, Buried trunks of Cinnamomum Camphora (L. Presl and their AMS^{14}C dates from Holocene alluvium deposits beneath the Kushima Plain, Miyazaki prefecture, Japan (in Japanese).

Nakamura, T., et al.: 2000, Nucl. Instrum. Methods Phys. Res. Sect. B 172, 52-57, The HVEE Tandetron AMS system at Nagoya University.

Nakamura, T.: 2003, RADIOISOTPES 52, 144-171, 加速器質量分析計 (AMS) によ

る環境中およびトレーサー放射性同位体の高感度測定 (in Japanese).

Pesnell, W.D.:2008, Solar Phys. 252, 209-220, Predictions of solar cycle 24.

Pinnegar, C.R. and Mansinha, L.: 2004, Signal Process. 84, 1167-1176, Time-local Fourier analysis with a scalable, phase-modulated analyzing function: the S-transform with a complex window.

Plunkett, G. and Swindles, G.T.: 2008, Quat. Sci. Rev. 27, 175-184, Determining the Sun's influence on Late glacial and Holocene climates: a focus on climate response to centennial-scale solar forcing at 2800 cal. BP.

Reimer, P.J., et al.: 2004, Radiocarbon 46, 1029-1058, 0-26 cal kyr BP, IntCal04 terrestrial radiocarbon age calibration.

Reimer, P.J., et al.: 2009, Radiocarbon 51, 1111-1150, IntCal09 and Marine09 radiocarbon age calibration curves, 0 - 50,000 years cal BP.

Richards, M.T., Rogers, M.L., and Richards, D.St.P.: 2009, Publ. Astron. Soc. Pac. 121, 797-809, Long-term variability in the length of the solar cycle.

Schwabe, S.H.: 1843, Astron. Nachr. 20, 283-288, Die Sonne. von herrn hofrath Schwabe.

Siegenthaler, U. and Beer, J.: 1988, Secular solar and geomagnetic variations in the last 10,000 years, Kluwer Academic Publishers, Boston, p. 315-328.

Solanki, S.K., Krivova, N.A., Schüssler, M., and Fligge, M.: 2002, Astron. Astrophys. 396, 1029-1035, Search for a relationship between solar cycle amplitude and

length.

Stockwell, R.G., Mansinha, L., and Lowe, R.P.: 1996, IEEE Trans. Signal Process. 44, 998-1001, Localization of the complex spectrum: The S transform.

Stuiver, M. and Polach, H.A.: 1977, Radiocarbon 19, 355-363, Discussion reporting of ^{14}C data.

Stuiver, M. and Quay, P.D.: 1980, Science 207, 11-19, Changes in atmospheric Carbon-14 attributed to a variable sun.

Stuiver, M. and Braziunas, T.F.: 1988, Secular solar and geomagnetic variations in the last 10,000 years, Kluwer Academic Publishers, Boston, p. 245-266.

Stuiver, M. and Braziunas, T.F.: 1989, Nature 338, 405-408, Atmospheric C-14 and century-scale solar oscillations.

Stuiver, M.: 1991, Quat. Res. 35, 1-24, Climatic, solar, oceanic, and geomagnetic influences on late-glacial and holocene atmospheric ^{14}C/^{12}C change.

Stuiver, M., et al.: 1998, Radiocarbon 40, 1041-1083, IntCal98 radiocarbon age calibration, 24,000-0 cal BP.

Swindles, G.T., Plunkett, G., and Roe, H.M.: 2007, J. Quat. Sci. 22(7), 667-679, A multiproxy climate record from a raised bog in County Fermanagh, Northern Ireland: a critical examination of the link between bog surface wetness and solar variability.

Usoskin, I.G., Solanki, S.K., and Kovaltsov, G.A.: 2007, Astron. Astrophys. 471, 301-309, Grand minima and maxima of solar activity: new observational constraints.

Usoskin, I. G., Sokoloff, D., and Moss, D.: 2009, Solar Phys. 254, 345-355, Grand minima of solar activity and the mean-field dynamo.

Watari, S.: 2008, Space Weather 6, 12, Forecasting solar cycle 24 using the relationship between cycle length and maximum sunspot number.

SWO PRF 1515: 2004, Space Weather Highlights 06-12 Sep 2004

Wainwright, M., Alshammari, M.F., and Alabri, K.: 2010, J. Cosmology 7, 1692-1702, Are microbes currently arriving to earth from space?